Title	Study on Internal Fracture and Anisotropic Inorganic Crystallization in Highly Stretched Double Network Hydrogels
Author(s)	深尾, 一城
Citation	北海道大学. 博士(生命科学) 甲第13947号
Issue Date	2020-03-25
DOI	10.14943/doctoral.k13947
Doc URL	http://hdl.handle.net/2115/78102
Type	theses (doctoral)
File Information	Kazuki_FUKAO.pdf

Doctoral Dissertation

Study on Internal Fracture and Anisotropic Inorganic Crystallization in Highly Stretched Double Network Hydrogels

（高延伸下ダブルネットワークゲルの内部破壊機構及び
異方的無機結晶の複合化に関する研究）

By

Kazuki Fukao

Supervisor: Jian Ping Gong,

Laboratory of Soft & Wet Matter,

Graduate School of Life Science, Hokkaido University

Sapporo 001-0021, Japan

March, 2020

Contents

CHAPTER 1: General introduction

Hydrogels, which consist of a three-dimensional polymer network stored a large amount of water, have interesting properties such as flexibility, transparency and low friction owing to its soft and wet properties. These properties close to the living soft tissues (cartilage, ligaments, tendons, muscles, etc.) compared to hard materials. Therefore, hydrogels are not only used in contact lenses and water absorbents, but is also being considered for application to next-generation biological substitute materials and tissue engineering substrates. However, synthetic hydrogels so far have extremely poor mechanical properties, and their application to structural materials where loads and tensions are applied is not realistic. In the synthesized hydrogels by a crosslinking reaction, the network structure is usually not uniform. When the force is applied to such hydrogels, the stress concentrates on a relatively short polymer chain between the cross-linking points, and initial crack is generated. The stress, then, continues to concentrate around the crack, resulting in hydrogels is ruptured rapidly due to the percolation of the crack.

Since the beginning of the 2000s, various strengthening strategies of hydrogels have been developed, and these strategies can be broadly classified as “uniformized of the force on polymer networks” and “sacrificial bond principle”. The former was accomplished by forming the extremely homogeneous polymer networks (Tetra-PEG hydrogels)[1] and introducing the cross-linking structure act as like a pulley (Slide-ring hydrogels)[2]. The latter strategy is explained that a weaker structure than the main structure of the material is introduced, and a large amount of energy are dissipated due to the preferentially fracture of the weak bond over a wide range during deformation, resulting in improving the toughness. Brittle and weak bonds are called sacrificial bonds and a typical example is the double network hydrogels (DN gels) developed in our laboratory[3,4].

A typical DN gel has an interpenetrated network structure consisting of two contrasting networks: one is brittle and weak, rupturing at small strain; and the other is stretchable and relatively strong, rupturing at significantly high strain and stress relative to the brittle one (**Figure 1-1**). Such contrasting DN structures were initially formed by a two-step synthesis process, in which a densely cross-linked polyelectrolyte was synthesized first as a brittle first network and then a sparsely cross-linked neutral polymer was synthesized as a stretchable second network in the presence of the brittle network. The DN strategy (sacrificial bond principle) has attracted significant attention as a method for developing strong and tough polymer materials including hydrogels[3-6] and elastomers[7,8], because this strategy is expressed by the contrasting mechanical properties of both networks and does not depend on the chemical species of the polymer.

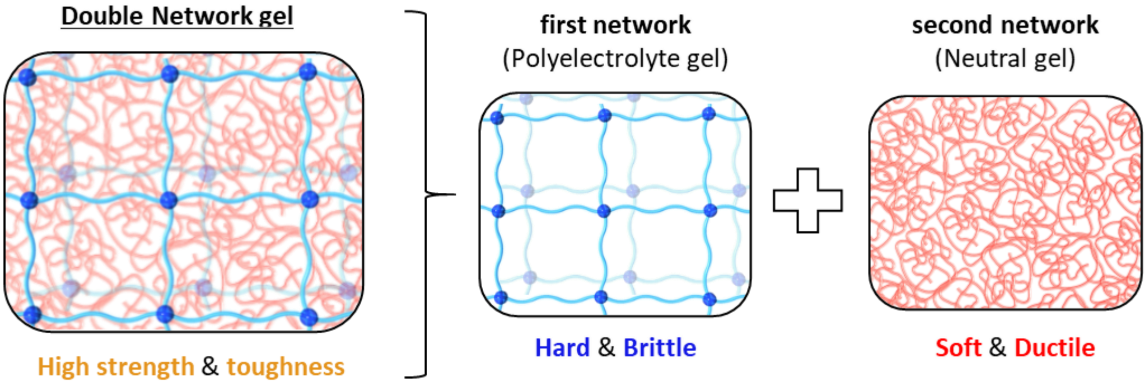

Figure 1-1. Schematic illustration of first (polyelectrolyte), second (neutral) and double network hydrogels, and each characteristic.

When tensile force is applied to a DN gel, the brittle first network strands are preferentially broken in a wide range as sacrificial bonds. However, the soft second network maintains unity of the material, thereby preventing the macroscopic failure of the material, resulting in high toughness of the DN gels. Because of this preferential internal fracture of the brittle network, tough DN gels usually show yielding behavior upon uniaxial deformation, in particular, distinct necking phenomenon often appears concomitant with the yielding.[9,10] Since the necked zone is softer than the unnecked zone, the necking phenomenon implies that the brittle network breaks and forms the discontinuous structure in the necked zone.[4,11,12] The above internal fracture mechanism of DN gels is proposed based on mechanical hysteresis, the anisotropic re-swelling after stretching, the electrostatic potential distribution and so on. However, the microscale and nanoscale structure evolution during the internal fracture process are still poorly known. Direct structure observation is therefore required to elucidate the fracture process of DN materials.

As described above, the main goal of this dissertation is to elucidate the internal fracturing process of the first network of DN gels during highly uniaxial stretching. This dissertation comprises five chapters including this general introduction as **Chapter 1**.

In Chapter 2, the background of this research is summarized from the aspects of scientific research including recent study. Firstly, the deformation and toughening mechanism of the DN gels based on the uniaxial tensile test is overviewed, and the expected fracturing mechanism in the DN gels described previous studies is explained. The internal structure of DN gels was also observed with relating to why the DN gels are tough using by using scattering method. Considering the previous research, the issues of revealing the internal fracturing of DN gels are extracted. As the strategy to overcome the issues, I applied high-brightness small angle X-ray scattering (SAXS) method, which can obtain the data at short irradiation time, to DN gels to evaluate the internal fracturing mechanism.

In Chapter 3, I elucidate the internal fracturing mechanism of DN gels, which shows yielding behavior during uniaxial stretching, by clarifying the internal structural change from different scales (nm and sub-μm scales). To evaluate the internal fracturing mechanism, I utilized DN gels composed of the second network with two different monomer concentrations were used while the composition of the brittle first network was fixed. Because it is known that tensile behavior of DN gels is depend on the mechanical balance between two networks.[9] Comparing the uniaxial tensile behavior of these two types of DN gels, both DN gels exhibited the yielding, and the DN gel with low second monomer concentration showed necking behavior during yielding. On the other hand, the DN gel with high second monomer concentration didn't show the necking behavior even beyond the yielding point.

On the analysis of SAXS profiles to extract the internal structure of DN gels, in this chapter, I focused on two internal structures; (1) the mesh structure of the brittle first mesh on nanometer scale and (2) the defects of the first network (voids) on the submicron scale. These structures were identified by the SAXS measurement on stretched DN gels using a high brightness synchrotron radiation facility (SPring-8, Japan). For obtained SAXS profiles at each stretch ratio of DN gels, the Ruland streak method was applied in low scattering vector, q, region (bigger structure) to calculate the long-axis length of the void along the stretch direction.[13,14] In addition, the Ornstein–Zernike function was applied to the SAXS profiles in high q region (smaller structure) to calculate the size of the mesh structure of the first network.[15,16] Based on the results from above analysis, I predicted the internal fracture mechanism of DN gel and discussed how and where the first network fractures and why the necking behavior of DN gels occurs related in on the mechanical balance, especially modulus, between brittle first and soft second networks.

In Chapter 4, applying the anisotropic internal structure of the first network on the stretched DN gels clarified in Chapter 3, I hybridized an anisotropic inorganic crystal with stretched DN gels by imitating the formation process of the bone tissue. Bone tissue forms an anisotropic composite structure consisting of collagen fiber as an organic template and hydroxyapatite (HAp) as a inorganic component, and the nucleation of HAp in the bone tissue is occurred on an anionic functional group of the organic template called as heterogeneous nucleation.[17] Moreover, some of reports was described that HAp grow anisotropically due to the spatial anisotropy formed by collagen template.[18,19] Therefore, in DN gels, I hypothesize follows; regioselective inorganic crystallization would occur on the first network having a sulfonic functional group. Then the anisotropic spatial distribution of the first network in stretched DN gels affect to the crystal growth direction.

To evaluate the influence of the first network distribution for crystal growth, in this chapter, I performed HAp mineralization in DN gels which controlled the spatial anisotropy of the first network by stretching at various stretch ratio, and the anisotropy of mineralized HAp was evaluated by wide angle X-ray diffraction (WAXD, SPring-8) quantitatively. Furthermore, the morphology of mineralized HAp and mechanical properties of DN gels mineralized anisotropic HAp is also investigated.

Finally, in **Chapter 5**, the conclusion and contributions of this research are summarized.

References

(1) Sakai, T.; Matsunaga, T.; Yamamoto, Y.; Ito, C.; Yoshida, R.; Suzuki, S.; Sasaki, N.; Shibayama, M.; Chung, U. Il. Design and Fabrication of a High-Strength Hydrogel with Ideally Homogeneous Network Structure from Tetrahedron-like Macromonomers. Macromolecules 2008, 41 (14), 5379–5384.

(2) Okumura, Y.; Ito, K. The Polyrotaxane Gel: A Topological Gel by Figure-of-Eight Cross-Links. Advanced Materials 2001, 13 (7), 485–487.

(3) Gong, J. P.; Katsuyama, Y.; Kurokawa, T.; Osada, Y. Double-Network Hydrogels with Extremely High Mechanical Strength. Advanced Materials 2003, 15 (14), 1155–1158.

(4) Gong, J. P. Why Are Double Network Hydrogels so Tough? Soft Matter 2010, 6 (12), 2583–2590.

(5) Sun, J. Y.; Zhao, X.; Illeperuma, W. R. K.; Chaudhuri, O.; Oh, K. H.; Mooney, D. J.; Vlassak, J. J.; Suo, Z. Highly Stretchable and Tough Hydrogels. Nature 2012, 489 (7414), 133–136.

(6) Myung, D.; Waters, D.; Wiseman, M.; Duhamei, P. E.; Noolandi, J.; Ta, C. N.; Frank, C. W. Progress in the Development of Interpenetrating Polymer Network

Hydrogels. Polymers for Advanced Technologies 2008, 19 (6), 647–657.

(7) Ducrot, E.; Chen, Y.; Bulters, M.; Sijbesma, R. P.; Creton, C. Toughening Elastomers with Sacrificial Bonds and Watching Them Break. Science 2014, 344 (6180), 186–189.

(8) Matsuda, T.; Nakajima, T.; Gong, J. P. Fabrication of Tough and Stretchable Hybrid Double-Network Elastomers Using Ionic Dissociation of Polyelectrolyte in Nonaqueous Media. Chemistry of Materials 2019, 31 (10), 3766–3776.

(9) Ahmed, S.; Nakajima, T.; Kurokawa, T.; Anamul Haque, M.; Gong, J. P. Brittle-Ductile Transition of Double Network Hydrogels: Mechanical Balance of Two Networks as the Key Factor. Polymer 2014, 55 (3), 914–923.

(10) Matsuda, T.; Nakajima, T.; Fukuda, Y.; Hong, W.; Sakai, T.; Kurokawa, T.; Chung, U. Il; Gong, J. P. Yielding Criteria of Double Network Hydrogels. Macromolecules 2016, 49 (5), 1865–1872.

(11) Na, Y. H.; Tanaka, Y.; Kawauchi, Y.; Furukawa, H.; Sumiyoshi, T.; Gong, J. P.; Osada, Y. Necking Phenomenon of Double-Network Gels. Macromolecules 2006, 39 (14), 4641–4645.

(12) Nakajima, T.; Kurokawa, T.; Ahmed, S.; Wu, W. L.; Gong, J. P. Characterization of Internal Fracture Process of Double Network Hydrogels under Uniaxial Elongation. Soft Matter 2013, 9 (6), 1955–1966.

(13) Thünemann, A. F.; Ruland, W. Microvoids in Polyacrylonitrile Fibers: A Small-Angle X-Ray Scattering Study. Macromolecules 2000, 33 (5), 1848–1852.

(14) Kawai, T.; Soeno, S.; Kuroda, S. ichi; Koido, S.; Nemoto, T.; Tamada, M. Deformation Induced Void Formation and Growth in β Nucleated Isotactic Polypropylene. Polymer 2019, 178 (June), 121523.

(15) Shibayama, M. Spatial Inhomogeneity and Dynamic Fluctuations of Polymer Gels. Macromolecular Chemistry and Physics. 1998, pp 1–30.

(16) Ryu, J.; Ko, J.; Lee, H.; Shin, T. G.; Sohn, D. Structural Response of Imogolite-Poly(Acrylic Acid) Hydrogel under Deformation. Macromolecules 2016, 49 (5), 1873–1881.

(17) Wang, Y.; Azaïs, T.; Robin, M.; Vallée, A.; Catania, C.; Legriel, P.; Pehau-Arnaudet, G.; Babonneau, F.; Giraud-Guille, M. M.; Nassif, N. The Predominant Role of Collagen in the Nucleation, Growth, Structure and Orientation of Bone Apatite. Nature Materials 2012, 11 (8), 724–733.

(18) Roveri, N.; Iafisco, M. Evolving Application of Biomimetic Nanostructured Hydroxyapatite. Nanotechnology, Science and Applications 2010, 3 (1), 107–125.

(19) He, G.; Dahl, T.; Veis, A.; George, A. Nucleation of Apatite Crystals in Vitro by Self-Assembled Dentin Matrix Protein 1. Nature Materials 2003, 2 (8), 552–558.

CHAPTER 2: Background

At first, I explain the tensile behavior of the typical DN gel under uniaxial tensile test until fracture. [1] **Figure 2-1** shows the stress-strain curve obtained from uniaxial tensile test and images of DN gels at each strain. The curve lineally increases in low strain region (A~C), and the brittle first network is broken but the fracture of the soft second network is not observed in this region. The stress yields at point of (C), and the necking phenomenon is often observed at yielding point. In the region of (D) The stress is constant even in increasing the strain and necked zone gradually propagates toward the clamps. After propagation of the necking over the entire specimen, increase the stress is observed during (E) and then, DN gels finally occur global rupture. On the global rupture, thus, the fracture of chemical bonds is needed not only at the fracture surface but also at thorough the material, resulting in DN gels exhibit the high toughness. Typical DN gels, consisting of poly(2-Acrylamido-2-methyl propanesulphonic acid) (PAMPS) as a first network and

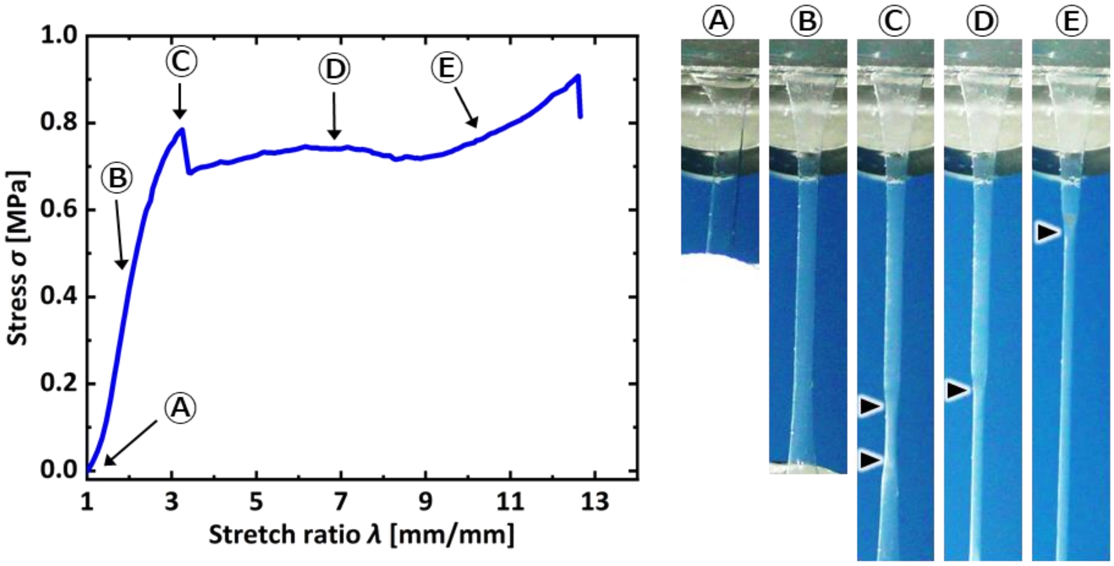

Figure 2-1. Stress-stretch ratio curve of PAMPS/PAAm DN gel under uniaxial tensile test, and pictures demonstrating the necking process. The insert alphabets represent the correspondence between the pictures and the arrowed data points.

poly(Acrylamide) (PAAm) as a second network, has the Young's modulus of 0.1 to 10 MPa, the fracture stress of 1 to 10 MPa, and the fracture strain of 1,000 to 2,000 %, despite with high water content (~90 wt%).

The change in polymer network at micro scale on above deformation process is described as follows. In the initial network structure in DN gels, the brittle first network strands are already fully-stretched state with entangle the loosely and soft second network. When the force is applied, DN gels exhibits high Young's modulus owing to the effect of fully-stretching (energetic elasticity), because the brittle network has little room for further stretch. The fracture of the first network is originated from the relatively short polymer strand, and this local fracture is occurred throughout the material with increasing the strain (A~C). This preferential fracture of the first network in the low strain is revealed from previous studies such as irreversible mechanical hysteresis[2] and chemical detection of bond breaking[3,4]. Although the independent local fracture of the first network percolates to the lateral direction in relative to the stretch direction and the large-scaled fracturing is formed at necking point of (C), the global fracture of DN gels is prevented by the existence of soft second network. Then, the necked zone become softer because the load at the necked regions is carried by the second network. Based on this phenomenon and the previous studies of anisotropic re-swelling after stretching[5] and electrostatic potential distribution[6], the fragmentation model, which the first network breaks into piece and forms the discontinuous structure, was proposed. However, the microscale and nanoscale structure evolutions during the internal fracturing process are still poorly known. Direct structure observations during deformation are therefore required to elucidate the fracture process in DN materials.

It is also roughly known that the tensile behavior of DN gels depends on the mechanical balance between brittle first network and flexible second network. For example, the tensile behavior of DN gels is different, especially around yield point, by changing second network density in DN gels (**Figure 2-2**). What causes this phenomenon? I focused on the origin and growth of cracks in DN gels during fracturing process. The initial structure of DN gels include defects of fist network called as "void" revealed by dynamic light scattering measurement of previous studies (**Figure 2-3**).[7-9] There is only second network in voids, and it is considered that the stress concentration occurs around voids because the modulus of second network is lower than that of pre-stretched first network. Therefore, I assume that the mechanical balance between two networks affects the stress concentration and growth of cracks, and I worked on revealing the internal fracturing process of DN gels with different second network density by using in-situ small angle X-ray scattering technique.

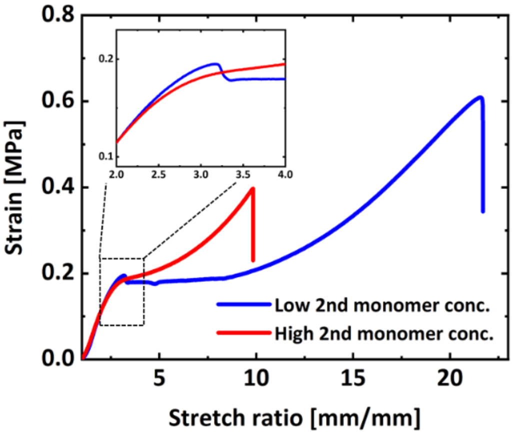

Figure 2-2. Stress-stretch ratio curves of DN gels with different second network density. Blue line is low second monomer concentration and red line is high second monomer concentration.

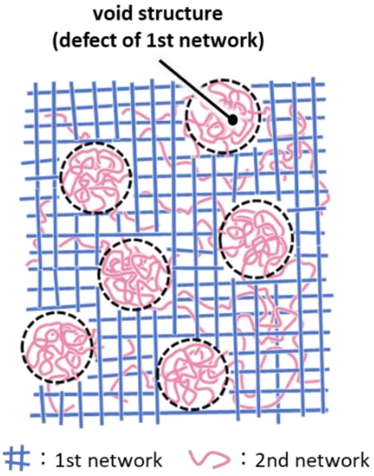

Figure 2-3. Illustration of void structure (defect of first network) in DN gels.

References

(1) Gong, J. P. Why Are Double Network Hydrogels so Tough? Soft Matter 2010, 6 (12), 2583–2590.

(2) Webber, R. E.; Creton, C.; Brown, H. R.; Gong, J. P. Large Strain Hysteresis and Mullins Effect of Tough Double-Network Hydrogels. Macromolecules 2007, 40 (8), 2919–2927.

(3) Ducrot, E.; Chen, Y.; Bulters, M.; Sijbesma, R. P.; Creton, C. Toughening Elastomers with Sacrificial Bonds and Watching Them Break. Science 2014, 344 (6180), 186–189.

(4) Matsuda, T.; Kawakami, R.; Namba, R.; Nakajima, T.; Gong, J. P. Mechanoresponsive Self-Growing Hydrogels Inspired by Muscle Training. Science 2019, 363 (6426), 504–508.

(5) Nakajima, T.; Kurokawa, T.; Ahmed, S.; Wu, W. L.; Gong, J. P. Characterization of Internal Fracture Process of Double Network Hydrogels under Uniaxial Elongation. Soft Matter 2013, 9 (6), 1955–1966.

(6) Guo, H.; Hong, W.; Kurokawa, T.; Matsuda, T.; Wu, Z. L.; Nakajima, T.; Takahata, M.; Sun, T.; Rao, P.; Gong, J. P. Internal Damage Evolution in Double-Network Hydrogels Studied by Microelectrode Technique. Macromolecules 2019, 52 (18), 7114–7122.

(7) Na, Y. H.; Kurokawa, T.; Katsuyama, Y.; Tsukeshiba, H.; Gong, J. P.; Osada, Y.; Okabe, S.; Karino, T.; Shibayama, M. Structural Characteristics of Double Network Gels with Extremely High Mechanical Strength. Macromolecules 2004, 37 (14), 5370–5374.

(8) Huang, M.; Furukawa, H.; Tanaka, Y.; Nakajima, T.; Osada, Y.; Gong, J. P. Importance of Entanglement between First and Second Components in High-Strength Double Network Gels. Macromolecules 2007, 40 (18), 6658–6664.

(9) Furukawa, H.; Kuwabara, R.; Tanaka, Y.; Kurokawa, T.; Na, Y. H.; Osada, Y.; Gong, J. P. Tear Velocity Dependence of High-Strength Double Network Gels in Comparison with Fast and Slow Relaxation Modes Observed by Scanning Microscopic Light Scattering. Macromolecules 2008, 41 (19), 7173–7178.

CHAPTER 3: Internal fracture mechanism of DN gels [1]

“Reprinted with permission from https://doi.org/10.1021/acs.macromol.9b02562. Copyright 2020 American Chemical Society."

3.1 Introduction

As shown in the general introduction, the main goal of my research is to elucidate the internal fracturing mechanism of the DN gels during highly uniaxial stretching. For direct observation of the polymer structure in hydrogels, the scattering method has been used. However, these previous measurements were performed for DN gels in non-stretched or low-strain state because of the strict measurement conditions such as a long irradiation time, drying hydrogels and so on. Therefore, the relationship between these estimated structures and the internal fracturing process as well as the yielding of the DN materials is still not known clearly. Although *in situ* small angle neutron scattering study on DN and TN elastomers in the pre-yielding regions has been reported recently, the results could hardly apply to the DN hydrogels that have quite different microstructure of the networks.[2]

In this chapter, I performed in situ small-angle X-ray scattering (SAXS) on DN gels at various stretch ratios up to the post-yielding region. From the SAXS measurement in SPring-8, the scattering data can be obtained at short irradiation time (<10s). DN gels from PAMPS as the brittle first network and poly(N,N-dimethylacrylamide) (PDMAAm) as the stretchable second network were used. We used two samples with the same first network formulation but different second network concentration, to study the effect of the mechanical balance of the two networks on the internal fracturing process and necking phenomenon in DN materials. The deformation of the nano-scale mesh and submicron-scale void in the first PAMPS network is extracted from SAXS results. The birefringence measurement was also performed to characterize the deformation of the dense second PDMAAm network. The observed results should help to understand the behavior of DN materials even without the void structure.

3.2 Experiments

3.2.1 Materials

2-Acrylamido-2-methylpropanesulfonic acid (AMPS) was procured from Toagosei Co. Ltd., Japan. N,N-Dimethylacrylamide (DMAAm), N,N'-methylenebisacrylamide (MBAA), and 2-oxoglutaric acid (α-keto) were purchased from FUJIFILM Wako Pure Chemical Corporation, Inc., Japan. All the chemicals, except DMAAm, were used without further purification. DMAAm was used after vacuum distillation.

3.2.2 Synthesis of PAMPS SN hydrogels

PAMPS single network (SN) gels were synthesized by free-radical polymerization from aqueous solutions containing 1 M AMPS as a monomer, x_1 mol% (to monomer) MBAA as a cross-linker, and 1 mol% (to monomer) α-keto as an initiator. The crosslinker concentration x_1 was varied from 1 to 8 mol% (typically 2 mol%). The solutions were injected into a mold consisting of a pair of glass plates separated by a 0.5 mm-thick silicone rubber. The PAMPS SN gels was synthesized by irradiating the mold with a ultraviolet (UV) lamp (wavelength 365 nm) for about 6 h under argon gas. The as-prepared PAMPS gels were used for the next step (**section 3.2.4**) to synthesize DN gels.

When the SN gel was used as the references, the as-prepared PAMPS SN gel was immersed in large amount of distilled water until reaching the swelling equilibrium.

3.2.3 Synthesis of PDMAAm SN hydrogels

PDMAAm SN gels were synthesized by free-radical polymerization from aqueous solutions containing 2 or 4 M DMAAm, 0.02 mol% MBAA, and 0.01 mol% α-keto, same as the **section 3.2.2**. The solutions were injected into a mold consisting of a pair of glass plates separated by a 1.5 mm-thick silicone rubber. The PDMAAm SN gels was synthesized by irradiating the mold with a UV lamp for about 8 h under argon gas. The obtained PDMAAm SN gels were used at as-prepared state, when the uniaxial tensile test and birefringence observation, and at swollen state, when SAXS measurement. The samples prepared from 2 M and 4 M DMAAm was coded as SN-2 and SN-4, respectively. The volume swelling ratios of SN-2 and SN-4 in swollen state relative to their as-prepared state were 2.01 and 4.38, respectively.

3.2.4 Synthesis of PAMPS/PDMAAm DN hydrogels

PAMPS/PDMAAm DN hydrogels were synthesized as follows. The PAMPS SN gels were firstly synthesized by above-mentioned method (**section 3.2.2**). The PAMPS SN gels were then immersed in an aqueous solution containing 2 or 4 M DMAAm, 0.02 mol% MBAA, and 0.01 mol% α-keto for 1 day until reaching the swelling equilibrium. The PAMPS network remarkably swelled in the DMAAm solution, and the volume swelling ratio of PAMPS gel in DMAAm solution relative to its as-prepared state was 32.77 and 28.09 for 2 M and 4 M DMAAm, respectively. The PDMAAm network was then synthesized by irradiating the PAMPS gels to obtain the PAMPS/PDMAAm DN gels. The samples prepared from 2 M and 4 M DMAAm were coded as DN-2 and DN-4, respectively. Before the measurement, the DN gels were immersed in distilled water for 1 week to remove any unreacted chemicals, and the distilled water was replaced twice daily. The DN gels further swelled in water, and the volume swelling ratios of DN gels relative to the as-prepared DN gels were 2.17 and 3.74 for DN-2 and DN-4, respectively. As a result, the PAMPS network was highly pre-stretched in the DN gels, having linear pre-stretch ratios in relative to its as-prepared state $\lambda_s = (32.77*2.17)^{1/3} = 4.14$ and $(28.09*3.74)^{1/3} = 4.72$, for DN-2 and DN-4, respectively. The monomer molar ratios of the second network to the first network were 65.54 and 112.38 for DN-2 and DN-4 samples, respectively. The volume changes of the first and second networks of DN gels are summarized in **Table 3-1**.

Table 3-1. Summary of the thickness, volume swelling ratio and the monomer molar concentration of the two networks during DN gels synthesis for DN-2 and DN-4,

		DN-2			DN-4		
		Thickness (mm)	Volume swelling ratio	Monomer molar conc. (M)	Thickness (mm)	Volume swelling ratio	Monomer molar conc. (M)
1st network	As-prepared	0.50	-	1.00	0.50	-	1.00
	Swell in DMAAm	1.60	32.77	0.03	1.52	28.09	0.04
	In swollen DN	2.07	70.96	0.01	2.36	105.15	0.01
2nd network	As-prepared	1.60	-	2.00	1.52	-	4.00
	In swollen DN	2.07	2.17	0.92	2.36	3.74	1.07

3.2.5 Uniaxial tensile test

Uniaxial tensile test was performed to evaluate the mechanical properties of DN-2, DN-4 and its corresponding SN gels. First, samples were cut into dumbbell shapes (15 mm gauge length and 10 mm width) by using the Laser cutter (PLS4.75, Universal Laser

Systems Inc.). Then, uniaxial tensile test was performed at a constant velocity of 100 mm/min by using a commercial tensile tester (Instron 5965, Instron Co.).

3.2.6 Birefringence measurement

To clarify the orientation of concentrated second PDMAAm network in the gels under uniaxial stretching, quantitative evaluation of birefringence was performed by a polarized optical microscope (Eclipse LV100N POL, Nikon Co., Japan) and the Berek compensator (Nichika Inc., Japan). Birefringence, Δn, was obtained by dividing the retardation value, R, by the sample thickness, d (i.e., $\Delta n = R/d$). The thickness d at each stretch ratio λ was measured by a thickness meter. To compare birefringence between samples with different second network concentrations, the normalized birefringence obtained by dividing Δn with the second monomer concentration, C_{2nd}, was adopted.

3.2.7 Small angle X-ray scattering (SAXS) measurement

SAXS measurements of the SNs and DN gels were performed at BL05XU of SPring-8 (Hyogo, Japan). The extremely high brightness of the undulator beamline permits fast data collection before causing distinct drying of hydrogels in air. The wavelength of the incident X-ray was 1 Å (12.4 keV in energy), and the sample-to-detector distance was 4 m. The gels of dumbbell shape (15 mm gauge length and 10 mm width) were set to the in-line tensile tester and were uniaxially stretched step-wise in the horizontal direction at a velocity of 2 mm/s from deformation ratio $\lambda = 1$ to fracture, with step width $\Delta\lambda = 0.5$ for $1 < \lambda < 2$ and $\Delta\lambda = 0.25$ for $\lambda > 2$. The exposure time of the sample to X-ray beam was 10 s for each λ. The scattering patterns were obtained via 2D detector PILATUS3 S 1M

(Dectris Ltd., Switzerland). The beam position on the gels was slightly changed at each λ to avoid any significant damage to the gels due to the X-ray exposure. Each experiment was performed at least on 3 samples to minimize the error.

3.2.8 Background subtraction and normalization for 2-dimentional SAXS images

The 2D scattering images were treated with background subtraction and normalization as follows. First, the transmittance of samples, T_s, to the X-ray beam was calculated from the incident beam intensity measured by the ionization chamber (IC) at sample stage IC_0 and the transmitted beam intensity was measured by a PIN diode embedded in the beam stopper IC_1.

$$T_s = \frac{(\mathrm{IC}_1^s - \mathrm{IC}_1^d)}{(\mathrm{IC}_1^a - \mathrm{IC}_1^d)} \bigg/ \frac{(\mathrm{IC}_0^s - \mathrm{IC}_0^d)}{(\mathrm{IC}_0^a - \mathrm{IC}_0^d)}$$

where superscripts s, a, and d stand for the beam intensities of the sample, air, and dark, respectively. Then, the scattering intensities of samples after thickness correction, I_{corr}, were obtained by image calculator processing on Image J (v1.49) software.

$$I_{corr} = \left(\frac{I_s}{T_s} - I_a\right) \times t_c$$

where I_s is the scattering image of the sample, I_a is air scattering image, and t_c is the thickness correction factor determined from the Lambert–Beer law using transmittance Ts at undeformed ($\lambda = 1$) and deformed (λ) states of the sample assuming that the density is constant under deformation.

$$t_c = \frac{\ln T_{s,\lambda=1}}{\ln T_{s,\lambda}}$$

The corrected 2D scattering images were converted into 1D intensity profiles by integrating the scattering intensity in the azimuth direction against the scattering vector q, defined as

$$q = \frac{4\pi}{\lambda} \sin \frac{\theta}{2}$$

where θ is the scattering angle calibrated by the diffraction pattern of dried collagen. The 1D intensity profiles for the directions perpendicular and parallel to stretching were obtained by integrating over azimuthal angles in the range of 90°±20° and 0°±20°, respectively.

3.2.9 Ornstein–Zernike function for identification of the size of first mesh structure

To calculate the mesh deformation ratio of the first network λ_{mesh} in two different directions, we fitted the Ornstein–Zernike (OZ) function on SAXS profiles of DN gels using Origin Pro software, as follows.

$$I(q) = \frac{I_0}{1 + \xi^2 q^2}$$

where I_0, ξ and q are the forward scattering intensity, the correlation length and scattering vector, respectively. The mesh deformation ratio λ_{mesh} was calculated based on the mesh size at global stretch ratio $\lambda = 1$ of the DN gels from following equation.

$$\lambda_{mesh} = \frac{\xi_{\lambda=x}}{\xi_{\lambda=1}}$$

3.2.10 Indentation test for identification of the size of first mesh structure

To calculate the mesh size of the first network, indentation test was carried out for as-prepared first SN gels (thickness: 3 mm) with different cross-linked density at 0.25 mm/min using a universal mechanical testing device (AUTOGRAPH AG-X, Shimadzu Co., Japan). The Young's modulus E was calculated using the Hertz model for indentation between indenter and sample, as follows.

$$h = \left[\frac{3}{4}\left(\frac{1-{\nu_1}^2}{E_1} + \frac{1-{\nu_2}^2}{E_2}\right)\right]^{\frac{2}{3}} \cdot F^{\frac{2}{3}} \cdot R^{-\frac{1}{3}}$$

where h, F, R, ν_1, ν_2, E_1 and E_2 are displacement, force, radius of indenter, Poisson ratio of indenter, Poisson ratio of sample, Young's modulus of indenter and Young's modulus of sample, respectively. In this study, R was 0.25 and ν_2 was assumed to be 0.5. When E_1 is much higher than E_2, the equation becomes following.

$$h = \left[\frac{3}{4}\left(\frac{1-{\nu_2}^2}{E_2}\right)\right]^{\frac{2}{3}} \cdot F^{\frac{2}{3}} \cdot R^{-\frac{1}{3}}$$

E_2 can be determined from the slope a of the $F^{2/3}$–h plot at the range of $h = 0.05 \sim 0.25$ mm.

$$a = \left[\frac{3}{4}\left(\frac{1-{\nu_2}^2}{E_2}\right)\right]^{-\frac{2}{3}} \cdot R^{\frac{1}{3}}$$

$$E_2 = \frac{3}{4}(1-{\nu_2}^2) \cdot R^{-1/2} \cdot a^{3/2}$$

The first network mesh size can be estimated using Young's modulus of sample E_2, as follows.

$$E_2 = \frac{3k_b T}{\xi_0^3}$$

$$\xi^3 = Q \times \xi_0^3$$

where k_b, T, ξ_0, ξ, and Q are Boltzmann constant, measurement temperature, mesh size of as-prepared first SN gels, mesh size of swollen first SN gels in DN gels, and volume swelling ratio of swollen DN gels relative to as-prepared first SN gels.

3.2.11 Ruland streak method for calculating the long-axis length of voids

To calculate the average void length $\langle L_{void} \rangle$ using Ruland streak method, the azimuth angle distribution at any scattering vector q was firstly obtained by using Fit_2D (v12.077) software, and the radian of full width at half maximum (FWHM) in azimuth direction of the streak at scattering vector q was calculated by fitting of Lorentzian function to the azimuth angle distribution using Origin Pro software. The void deformation ratio λ_{void} was calculated from following equation.

$$\lambda_{void} = \frac{\langle L_{void\,(\lambda=X)} \rangle}{\langle L_{void\,(\lambda=1)} \rangle}$$

where $\langle \boldsymbol{L_{void\,(\lambda=1)}} \rangle$ is the void length at $\lambda_{\text{DN}} = 1$. Since $\langle \boldsymbol{L_{void\,(\lambda=1)}} \rangle$ cannot be obtained from the Ruland streak method, we estimated $\langle \boldsymbol{L_{void\,(\lambda=1)}} \rangle$ of DN-4 by extrapolating the linear relation between the $\langle L_{void} \rangle$ and λ to λ=1. The $\langle \boldsymbol{L_{void\,(\lambda=1)}} \rangle$ of DN-2 was calculated from $\langle \boldsymbol{L_{void\,(\lambda=1)}} \rangle$ of DN-4 by considering the volume swelling ratio difference between the two DN gels.

3.3 Results & discussion

3.3.1 Uniaxial tensile behavior and normalized birefringence

Figure 3-1(a) shows the tensile behaviors of the two DN gels synthesized from the same first network but with two different second monomer concentrations. Their stress (σ)-stretch ratio (λ) curves overlap at low λ, and both of them show yielding behavior. However, their σ-λ curves deviate from each other at large λ (>2), showing significantly different yielding behaviors. For the DN-2 gel with low second monomer concentration, a clear stress peak appeared at the yield point and the necking phenomenon was observed after yielding (**Figure 3-1(b-i)**). The stress in the DN-4 gel with high second monomer concentration saturated at the yielding point, and the sample deformed homogeneously without showing the necking behavior (**Figure 3-1(b-ii)**). These results clearly indicate that the yielding and necking behaviors of DN gels depend on the second network concentration that changes the mechanical balance between the two networks, although the second network alone is much softer than the DN gels, as seen in **Figure 3-1(a)**.

When the internal rupture in the first network occurs in DN gels, the load carried by these broken strands is partly transferred to the second network, inducing microscopic stretching and orientation of the second network along the tensile direction. This effect can be observed from the change in the birefringence of the DN gels during stretching, because the second monomer molar concentration in the DN gel is more than 60 times higher than in the first network. **Figure 3-1(c)** shows the normalized birefringence for the two DN samples and their corresponding second SN gels. For the same second network concentration, the birefringence of the DN samples is slightly stronger than their corresponding SN gels at small λ ($1<\lambda<3$), and gradually increases with λ. However, birefringence of the DN samples becomes distinctly stronger than their corresponding SN gels when λ is beyond the yielding point ($\lambda>3$). In particular, the birefringence of DN-2 in the necking region rapidly increases above the yielding point and becomes significantly higher than its corresponding SN, indicating significant local orientation of the second network in the necking region. On the other hand, the birefringence of DN-4 that shows homogeneous deformation gradually increases even above the yielding point, showing a modest increase than its corresponding SN gel above the yielding point. These results again confirm the strong local orientation of the second network in DN-2 but not in DN-4 by yielding. The stronger birefringence of DN-4 (or SN-4) than DN-2 (or SN-2) even after normalization by the second network concentration should be attributed to the enhanced entanglement of the sample prepared at the higher concentration. These mechanical and optical results suggest different fracturing processes and structure evolutions for the two DN gels under uniaxial extension. Above the yielding point, the first network of the DN-2 sample, which shows necking, breaks into discontinuous structure and the load between the discontinuous regions is carried by the second network, which induces local strain amplification and strong orientation of the second network. In contrast, the first network of the DN-4 sample still has a continuous structure above the yielding, without local strain amplification and strong second network orientation.

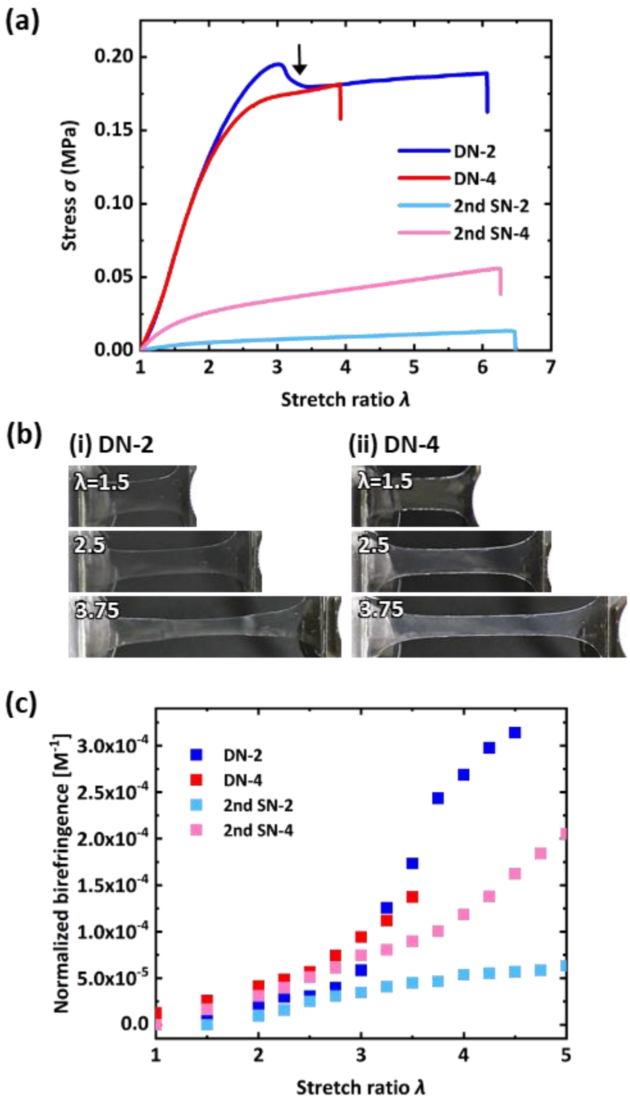

Figure 3-1. (a) Uniaxial tensile stress-stretch ratio curves of the DN gels with different second monomer concentration and its corresponding 2nd SN gels. The arrow indicates starting point of necking. (b) The optical images of (i) DN-2 and (ii) DN-4 gels under uniaxial stretching. (c) Normalized birefringence of DN-2, DN-4 and its corresponding second SN gels under uniaxial stretching. The second SN gels were used at as-prepared state.

3.3.2 SAXS measurement on swollen SNs and DN gels

SAXS results for the undeformed first SN, second SN, and DN gels in swollen state are shown in **Fig.3-2(a-b)**, where DN-2 and its corresponding SN were used as typical examples. Isotropic scattering images are observed in all cases (**Figure 3-2(a))**. The 1D scattering profiles can be divided into high-q and low-q regions (**Figure 3-2(b)**). In the high-q region (typically $0.2 < q < 1$), the profiles of the DN gels obey the Ornstein–Zernike (OZ)-type scattering behavior:

$$I(q) = \frac{I_0}{1 + \xi^2 q^2}$$

where I_0, ξ, and q are the forward scattering intensity, correlation length, and scattering

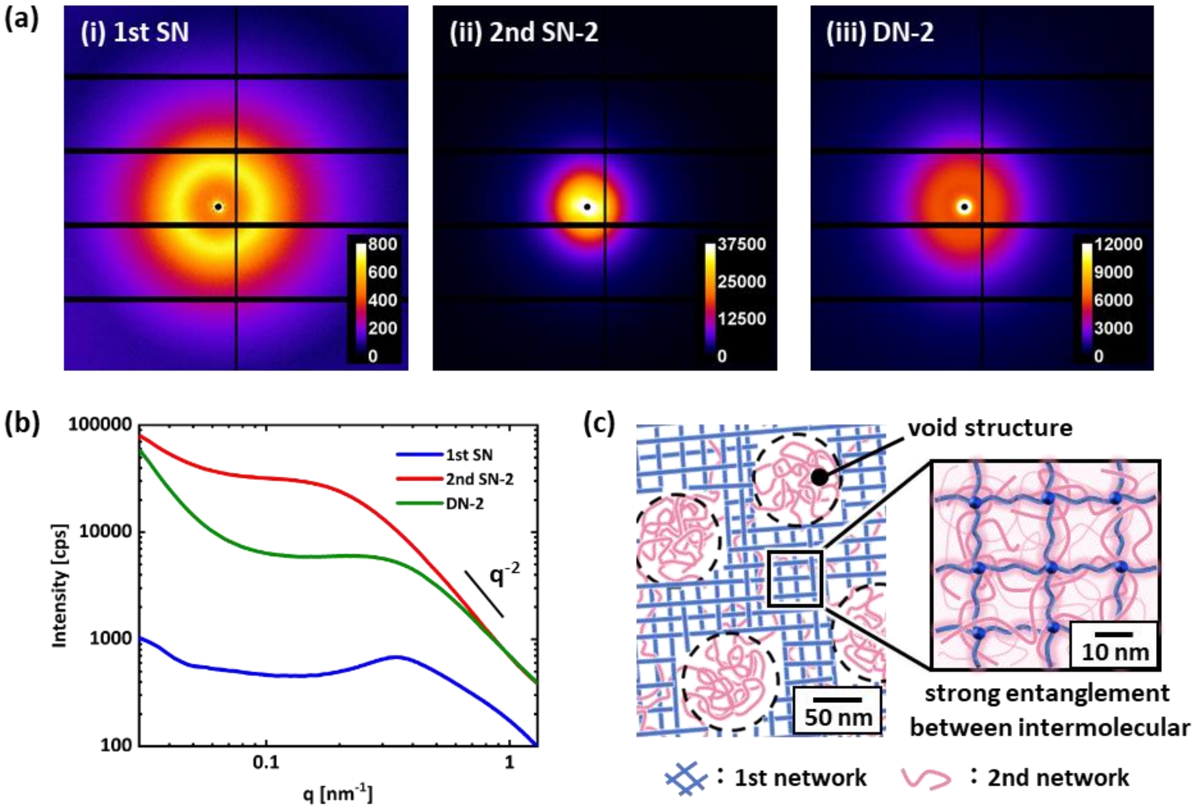

Figure 3-2. (a) 2-dimensional SAXS images of (i) first PAMPS SN gel, (ii) second PDMAAm SN-2 gel, and (iii) DN-2 gel at their undeformed state. (b) 1-dimensional SAXS profiles of these gels obtained from the 2D images. (c) Schematic illustration of a DN gel containing voids in the first network. The second network strongly entangles with the first network.

vector, respectively. The OZ-type scattering behavior, originating from the concentration fluctuation of the polymer strands, is typically found in the scattering profile of polymer solutions and gels.[3-6] The correlation length, ξ, is related to the shoulder position in the 1D scattering profiles; the shoulder at lower q means larger ξ. Comparing the scattering profiles of SNs, we found that the shoulder of the second SN profile is located toward lower q than the first SN profile, which relates to larger ξ of the second SN than that of the first SN. In addition, a small peak (so called polyelectrolyte peak) was found in the first SN profile owing to the polyelectrolyte nature of the first network.[7-9] For the SAXS profile of the DN gel, scattering should originate from the second network, because the concentration of the second network was much higher than that of the first network in the DN gels. However, the scattering vector q at the shoulder position in the 1D profiles of the DN gel is much closer to that of the first network than that of the second network. This suggests that the concentration fluctuation of the second network, which corresponds to the correlation length of the DN gels, is controlled by the mesh of the rigid first network as a skeleton through strong entanglement between the first and second networks (**Figure 3-2(c)**). A similar hypothesis has also been indicated based on the DLS measurement.[10] To confirm this hypothesis, we performed SAXS measurements on the DN-2 gels having varied first network cross-linking densities (**Figure 3-3(a)**). Although the second network composition of these DN gels is the same, the shoulder position in the scattering profiles shifts to higher q when the first network cross-linking density increases, indicating that the first network mesh size becomes smaller with an increase in the cross-linking density. Furthermore, the correlation lengths ξ of the DN gels calculated from the scattering profiles using OZ-type function well agreed with the mesh sizes of their corresponding single first network obtained from the mechanical measurements (**Figure 3-3(b)**). Based

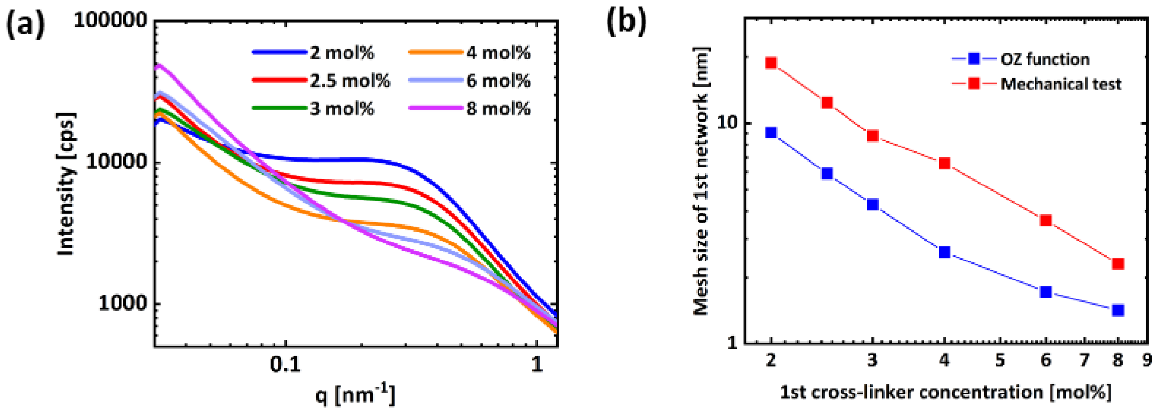

Figure 3-3. (a) SAXS 1D profiles of swollen DN gels with various concentration of the first network cross-linker. (b) Comparison of the mesh size of the first network obtained from OZ function fitting and indentation test.

on these investigations, we conclude that the OZ-type scattering profiles of the DN gels in the high-*q* region reflect the nanometer-scale mesh structure of their first network.

In the low-q region (typically $0.035 < q < 0.2$), large anomalous scattering appears on the scattering profile of the gels, which indicates the existence of a large-scale structure. In particular, most significant anomalous scattering was observed on the SAXS profile of the DN gel, suggesting an enhancement of the large-scale inhomogeneity in the second network by forming the double network structure. We believe that the enhanced inhomogeneity in the second network of the DN gel originates from preexisting voids of the first network in the DN gel. The previous DLS studies on DN gels suggested submicrometer-scale voids in the first network of the DN gels, and the second network in the voids showed slower cooperative diffusion than the second network in the mesh of the first network.[11,12] It is consistent with the assumption that the void region has a lower shear modulus than that of the non-void region. This is because the cooperative diffusion coefficient is positively related to shear modulus μ and bulk modulus K of the gel. Shear modulus μ, which depends on the cross-linking density, should be significantly higher in the mesh region than in the void region because of the strong entanglement of the second network to the first network. Based on these investigations, we conclude that the anomalous scattering of DN gels in the low-*q* region reflects the submicrometer-scale void structure of their first network (**Figure 3-2 (c)**).

3.3.3 in-situ SAXS analysis of DN gels under uniaxial stretching

The above discussion suggests that one can extract nanometer- and submicrometer-scale structural information of the first network from the SAXS profiles of the DN gels. Subsequently, in situ SAXS measurements on the uniaxially deformed DN-2 gel was performed to investigate the stretching-induced structural changes in the two different scales **(Figure 3-4)**. The 2D SAXS images of the DN-2 gel at different stretching ratios are shown in **Figure 3-5(i)**. The scattering patterns of the DN gels changed from isotropic to streak with an increase in stretch ratio λ. This pattern transition to the streak indicates a change in the submicrometer-scale void structure from the isotropic shape to anisotropic ellipsoidal shape on stretching. To investigate the changes in the mesh size in the directions parallel and perpendicular to the stretching direction, 1D profiles in the directions parallel and perpendicular to the tensile deformation were obtained by angle-

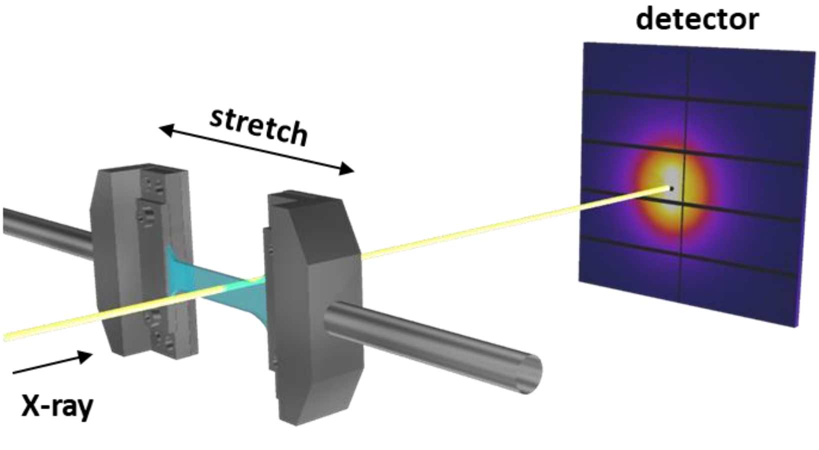

Figure 3-4. (a) Schematic of SAXS measurement geometry.

selective integration. As seen in **Figure 3-5(i)**, in the high-q region, the scattering profiles relating to the nanometer-scale mesh size of the first network still obey the OZ-type pattern regardless of the stretch ratio, thereby suggesting that the first network mesh structure is hardly changed in the deformed DN-2 gels. However, the shoulder in the scattering profile of the deformed DN gels slightly shifts with an increase in stretch ratio λ. The shoulder in the parallel profiles shifts to lower q, whereas that in the perpendicular profiles shifts to higher q with the stretching ratio. These results are qualitatively consistent with the common behavior that the mesh of the (first) network is elongated parallelly but compressed perpendicularly to the direction of stretching. The DN-4 gel also shows a streak pattern at large deformation and the shifts of the shoulders towards opposite q directions in the parallel and perpendicular 1D profiles (**Figure 3-5(ii)**).

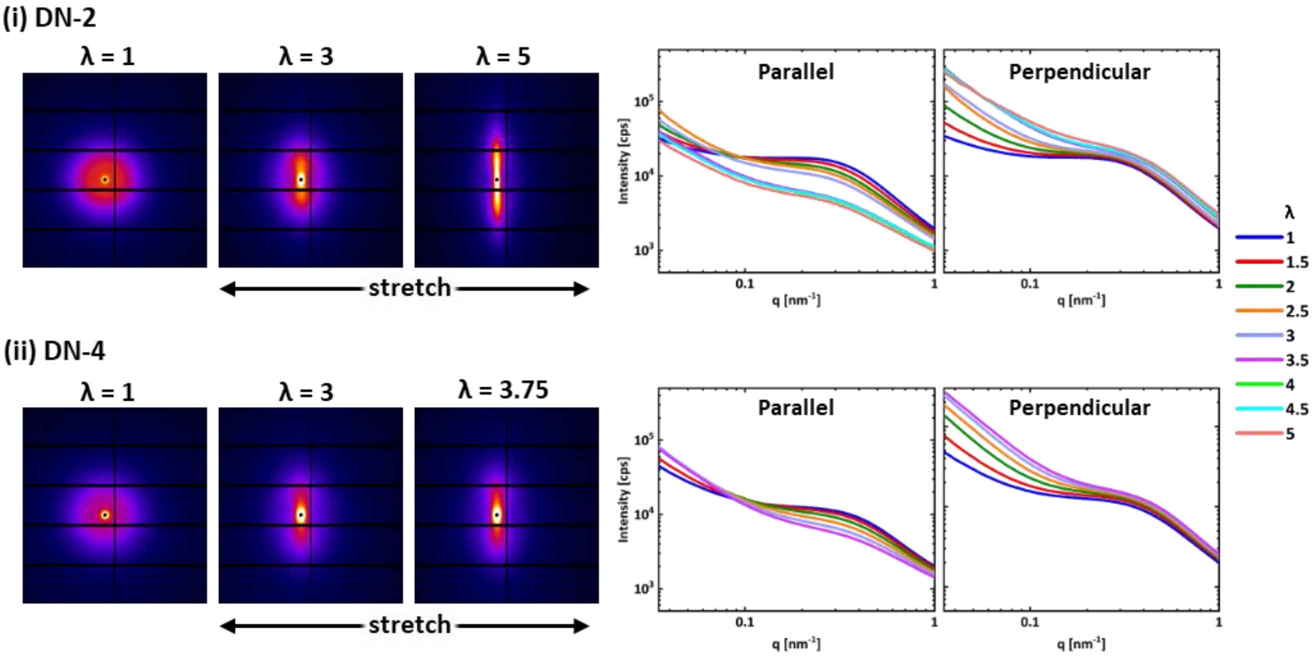

Figure 3-5. Representative 2D SAXS images and 1D SAXS profiles of the (i) DN-2 and (ii) DN-4 samples under uniaxial stretching. 1D profiles were obtained from parallel and perpendicular directions in relative to the tensile deformation. Above the yielding point, the results of DN-2 are for their necking region.

Focusing on these changes in the scattering data of DN gels, we quantitatively evaluated the structural change in the DN gels upon uniaxial deformation in different size scales using two types of analysis methods. First, we analyzed the submicrometer-scale void structure using the Ruland streak method. This method has been widely used to analyze oblong structures such as shish and void lengths.[13-16] For azimuthal distributions of the streak that obey the Lorentz function, the average void length $\langle L_{void} \rangle$ and azimuthal width owing to misorientation of voids B_{φ} are described by the following equation using the Ruland method:

$$qB_{obs} = \frac{2\pi}{\langle L_{void} \rangle} + qB_{\varphi}$$

where B_{obs} represents the radian of full width at half maximum in the azimuth direction of the streak at scattering vector q. From above equation, the qB_{obs} versus q plot shows a linear line, and $\langle L_{void} \rangle$ and B_{φ} can be obtained from the intercept ($=2\pi/\langle L_{void} \rangle$) and slope of the linear line, respectively. Furthermore, the orientation degree of voids, f_{void}, can be calculated from

$$f_{void} = \frac{180 - B_{\varphi}}{180}$$

We have confirmed that the Lorentz function fits well the azimuthal distributions of streak peaks of DN gels in the range of 70°–110°, and the qB_{obs} versus q plots at various stretch ratios λ shows a good linearity in the low-q region (**Figure 3-6**). Therefore, we applied the Ruland method to analyze our streak patterns.

The dependence of the void length along the stretch direction, $<L_{void}>$, of DN gels on stretch ratio, λ, is shown in **Figure 3-7 (a)**. For DN-2, $<L_{void}>$ first increased gradually with λ then increased rapidly near the necking point. After reaching the necking

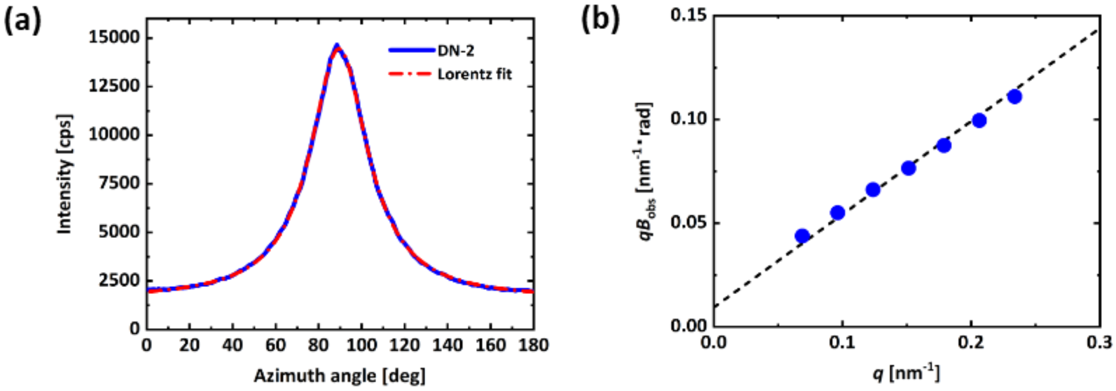

Figure 3-6. (a) Azimuth angle distribution of DN-2 and the Lorentz fitted line. (b) The linear plot between the qB_{obs} and q.

point, $<L_{void}>$ decreased and became constant during necking propagation. In contrast, the $<L_{void}>$ of the DN-4 gel increased only weakly with λ until the sample fractured, without showing any significant increase near the yielding point. The dependence of the orientation degree of voids, f_{void}, on stretching ratio λ is shown in **Figure 3-7 (b)**. The f_{void} of DN-2 also showed a rapid increase near the necking point and became constant during necking propagation; whereas f_{void} of the DN-4 gel increased linearly with the global deformation until the sample failure.

To compare the macro-scale deformation with micro-scale deformation, the void deformation ratio along the stretch direction, λ_{void}, was evaluated based on $\langle L_{void}\rangle$ at $\lambda = 1$. The estimation method for $\langle L_{void}\rangle$ at $\lambda = 1$ is shown in the Supporting Information. **Figure 3-7 (c)** shows the void stretching ratio, λ_{void}, as a function of global stretch ratio λ. The λ_{void} of DN-2 gel is significantly larger than the affine deformation prediction. It increases nonlinearly with λ, particularly around $\lambda = 2.25–3.25$, and decreases abruptly at yielding. In contrast, λ_{void} of the DN-4 gel is slightly weaker than the affine deformation prediction. The extraordinary non-affine deformation of voids in the DN-2 gel indicates that deformation is highly localized around the voids in DN-2 gel; however, it is not so in the

DN-4 gel.

Next, the deformation of the nanometer-scale mesh of the first network was evaluated. The 1D parallel and perpendicular profiles in the high-q region were fitted by the OZ functions and lengths ξ were determined based on the mesh sizes of the first network in the two directions. The mesh deformation ratio of the first network, λ_{mesh}, was evaluated based on the mesh size at λ = 1. **Figure 3-7 (d)** shows the local mesh deformation ratio of parallel ($\lambda_{mesh,p}$) and vertical ($\lambda_{mesh,v}$) directions as a function of the

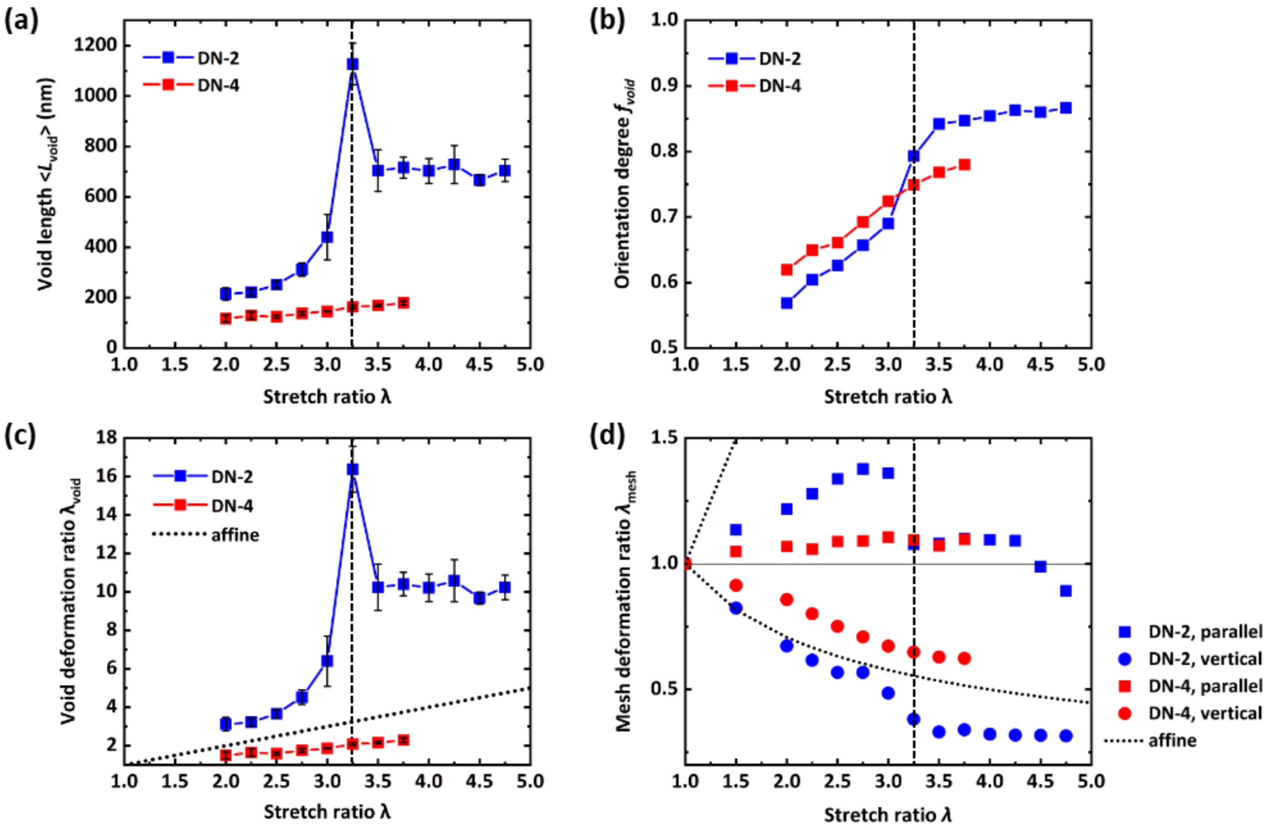

Figure 3-7. Structure evolution of the DN-2 and DN-4 samples as a function of global stretch ratio. The dashed line at λ=3.25 indicates the stretch ratio at the necking point for DN-2. (a) Long-axis length of voids. (b) Orientation degree of voids. (c) Void deformation ratio λ_{void}. (d) Mesh deformation ratio λ_{mesh} of the first network. The dotted lines denote the affine deformation prediction. For DN-2 sample in necking regime, the results are obtained from the necked region.

global stretch ratio λ of the DN gels. For DN-2, $\lambda_{mesh,v}$ in the vertical direction almost follows the affine deformation until reaching necking, and a sudden decrease in $\lambda_{mesh,v}$ with yielding is observed. In contrast with $\lambda_{mesh,v}$, the deformation behavior, $\lambda_{mesh,p}$, in the parallel direction does not obey affine deformation. Before reaching the yielding point, $\lambda_{mesh,p}$ increased with the global λ; however, its value was significantly smaller than the affine deformation, and $\lambda_{mesh,p}$ also suddenly decreased at the yielding point. The $\lambda_{mesh,v}$ and $\lambda_{mesh,p}$ of the DN-4 gel were both smaller than the affine deformation, without showing sudden changes at the yielding point.

3.3.4 Expected fracturing evolution mechanism

Based on the nanometer-scale mesh deformation and submicrometer void deformation, we first discuss the structure of the DN-2 sample that shows necking. The sub-affine deformation of the mesh along the stretch direction indicates heterogeneous deformation of the samples and should be attributed to the internal fracturing of the first network. As shown by mechanical hysteresis, the internal fracturing of the first work starts to occur even at small λ (~1.5), far below the yielding point.[17,18] Because the first network strands are in highly pre-stretched state by swelling (λ_s = 4.14), the deformation capacity of the first network mesh in the DN gel is very small. So some of the first network strands start to rupture at very small stretch. As a result, the second network in the fractured first network region is largely stretched. The strain amplification in the fractured region largely compensates the less deformable mesh remaining in the first network to show a smaller mesh deformation ratio along the stretching direction than the affine deformation. Interestingly, $\lambda_{mesh,p}$ rapidly returns to the undeformed value at the necking point (λ = 3.25) where necking starts to occur, which suggests that the first network was unloaded by the formation of the discontinuous structure (fragmentation) at the yield point. It implies that most of the stress in the DN-2 gel, after necking, is carried by the stretchable second network. Such observed local unloading of the first network is consistent with the fragmentation model of the first network proposed in previous studies.[19-21] From the large void deformation ratio along the stretch direction, λ_{void}, the fracturing in the first network occurs from the pre-existing voids. Previous studies on swelling anisotropy indicate that selective fracturing of the first network propagates in the direction perpendicular to stretching.[21-23] Therefore, the fracturing in the first network occurs from lateral edges of voids because of stress concentration, along the direction vertical to the tensile deformation.

Next, we discuss the structure of the DN-4 sample. The sub-affine deformation of the voids as shown in **Figure 3-7(c)** indicates that the stretching-induced fracturing of the first network occurs homogeneously in the sample and is not localized around the voids even beyond the yielding point. This indicates that the internal fracturing process and mechanical behavior become less or even insensitive to voids, and the fracture occurs dispersedly over the entire sample, resulting in the yielding without necking. Because the second network at the fractured points of the first network deforms only modestly, we observe only small increase in the birefringence of the DN-4 as compared with its corresponding SN in **Figure 3-1(c)**. As shown in **Figure 3-7(d)**, the DN-4 showed less deformation of mesh both in the directions parallel with ($\lambda_{mesh,p}$) and vertical to ($\lambda_{mesh,v}$) the stretching, in comparison with those of the DN-2 gel. This could be attributed to the larger pre-stretch of the first network strands in the DN-4 gel (λ_s = 4.72 for DN-4 vs λ_s = 4.14 for DN-2) due to more larger swelling in the higher second monomer concentration.

Figure 3-8 schematically illustrates the elucidated structural changes in uniaxially deformed DN gels with different second network concentration. As shown in **Figure 3-8(a)**, the existence of first network void induces stress concentration around the void owing to differences in moduli between the non-void region where the modulus is dominated by the rigid first network and void region where only the soft second network exists. The fracturing process of the first network in DN gels depends on the modulus (E) and stretch ability (λ_m) differences between the first network (E_1 and $\lambda_{m,1}$) and the second network (E_2 and $\lambda_{m,2}$). For a fixed first network, the modulus ratio E_1/E_2 increases while stretch ability ratio $\lambda_{m,1}/\lambda_{m,2}$ decreases with the decrease of the second network concentration. At low second network concentration (DN-2), $E_1/E_2>>1$, so initial fracture in the first network occurs near the lateral edge of the voids by the stress concentration, and the fracture grows in the direction vertical to the stretch due to the relatively high stretching ability of the second network, which leads to anomalous void extension. On the other hand, at high second network concentration (DN-4), $E1/E_2\geq 1$, and the fracture also occurs near the lateral edge of the voids, similar to DN-2, but the stress concentration is largely suppressed, because the strain hardening of the second network occurs at relatively smaller stretching owing to its increase in the self-entanglement. As a result, the first network fracture also occurs in non-void region to show homogeneous fracture in the sample

As illustrated by the internal fracturing process of the DN gels in **Figure 3-8(b)**, when tensile force is applied to the DN gels with relatively low second monomer concentration ($E_1>>E_2$), the pre-stretched first network strands are selectively fractured near the lateral edges of voids, which induces remarkable stretching of the soft second network to carry the load, as seen by the significantly stronger birefringence in comparison with its corresponding SN gel in **Figure 3-1(c)**. The local strain amplification by fracturing of the first network makes the voids deform more than the affine deformation. With the progress of stretching, such regioselective internal fracturing of voids induces percolation of the fracture in the lateral direction, resulting in the necking behavior and unloading of the first network. At an elevated second monomer concentration ($E_1 \geq E_2$), the modulus of the second network increases and the stretching ability decreases owing to its increase in the self-entanglement, resulting in the suppression of the stress concentration near the voids.

The proposed internal fracturing scenario in **Figure 3-8** suggests that the key reason for the necking of DN gels is the sufficiently large contrasts in moduli and extensibilities between the two networks, which induces significant strain amplification around the voids (or defects). Even for the relatively homogeneous first network not containing the submicrometer-scale voids, necking should also occur when the stress concentration is sufficiently strong. As seen in the DN gels with the tetra-PEG first network that does not contain large-scale spatial inhomogeneity, necking occurs when the second network is relatively soft.[24,25] This is because there should be small-scale defects even in the tetra-PEG network, which can induce local strain amplification near the defects and lead to propagation of first network fracture to show necking.

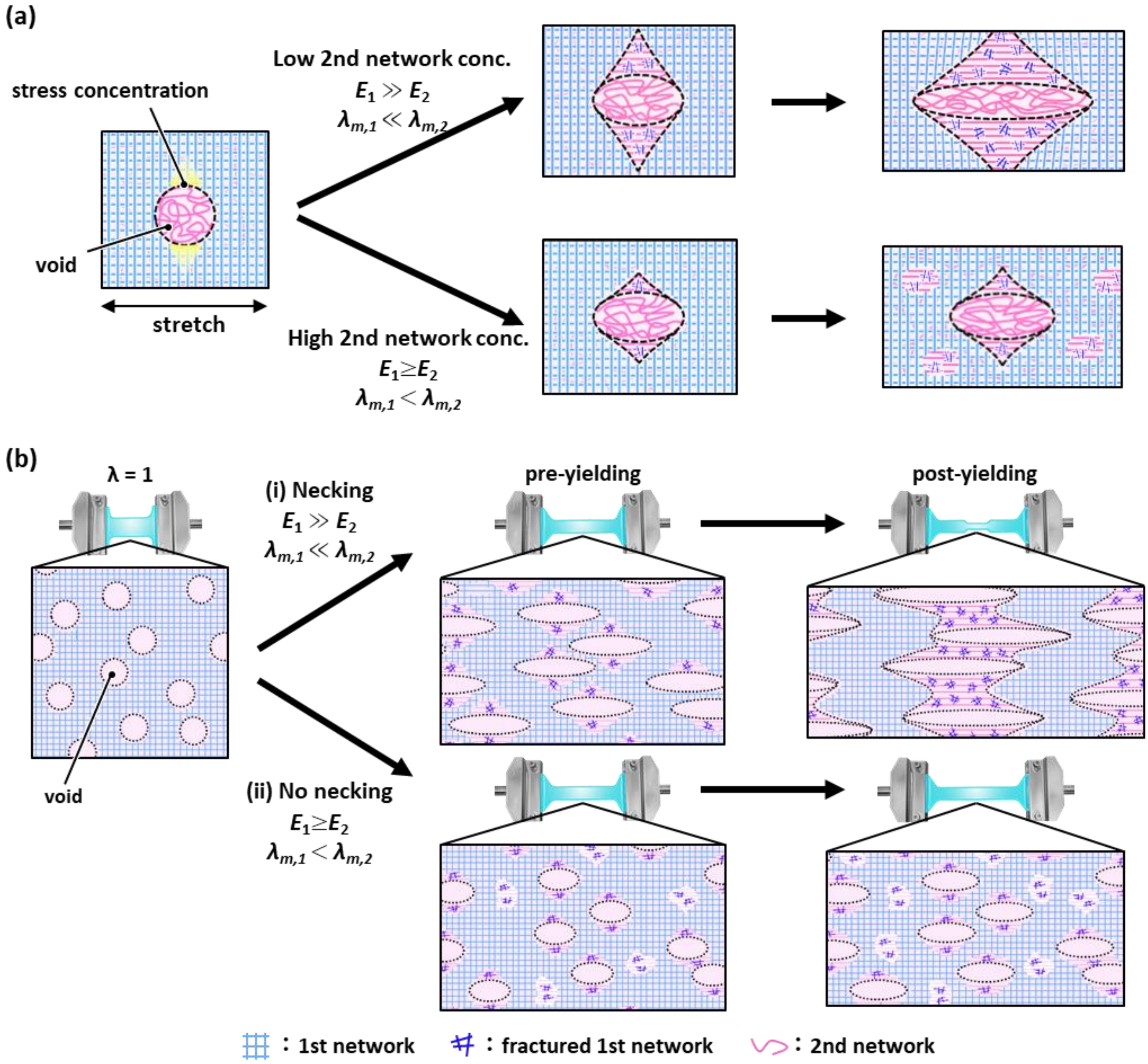

Figure 3-8. Schematic illustration of fracturing process of the first network in DN gels with different second network concentration. (a) Stress concentration and first network fracture around the void (defect) depend on the difference in modulus (*E*) and stretch ability (λ_m) between the first (E_1 and $\lambda_{m,1}$) and second (E_2 and $\lambda_{m,2}$) networks, respectively. For a constant structure of the first network, the ratio E_1/E_2 and $\lambda_{m,2}/\lambda_{m,1}$ increases with the decrease of second network concentration. DN gel with low second network concentration has a strong stress concentration around the lateral edge of void to cause fracture with large crack opening of the first network in the direction vertical to the stretch, while the DN gel with high second network concentration has weak stress concentration and small crack opening around the void, so the first network fracture occurs also in non-void region. (b) DN gel with strong stress concentration causes necking behavior (i) and DN gel with weak stress concentration does not (ii) under uniaxial tensile process. The second network in the mesh regions is shown by pink color. When $E_1/E_2>>1$, the fracture of first network, starting from the lateral edge of the voids, propagates in the direction vertical to the tensile deformation, to form fragment structure, resulting the necking behavior of the DN gels. Such fracture process leads to anomalous void extension. When $E_1/E_2 \geq 1$, the stress concentration near the voids is suppressed and the first network fractures homogeneously in the sample, even at post-yielding region.

3.4 Conclusions

We investigated structural changes in DN gels under uniaxial stretching, both in nanometer- and submicrometer-scale by SAXS measurements. We found that the mechanical balance between the two networks determines the internal fracturing process in DN gels. For the DN-2 gel with significant differences in moduli and stretch abilities between the two networks, internal fracturing is initiated near the voids in the lateral direction and propagated along the direction vertical to the stretching; and percolation of the fracture in lateral direction triggers necking of the sample. For the DN-4 gel with relatively less differences in moduli and stretch abilities between the two networks, internal fracturing occurs dispersedly over the sample, irrespective of the presence of voids. This study deepens the understanding on the toughening and yielding mechanisms of DN systems, which is useful for designing DN gels with desired mechanical properties for various applications.

3.5 References

(1) Fukao, K.; Nakajima, T.; Nonoyama, T.; Kurokawa, T.; Kawai, T.; Gong, J. P. Effect of Relative Strength of Two Networks on the Internal Fracture Process of Double Network Hydrogels As Revealed by in Situ Small-Angle X-Ray Scattering. Macromolecules 2020. https://doi.org/10.1021/acs.macromol.9b02562.

(2) Ducrot, E.; Montes, H.; Creton, C. Structure of Tough Multiple Network Elastomers by Small Angle Neutron Scattering. Macromolecules 2015, 48 (21), 7945–7952.

(3) Shibayama, M. Spatial Inhomogeneity and Dynamic Fluctuations of Polymer Gels. Macromolecular Chemistry and Physics. 1998, pp 1–30.

(4) Chalal, M.; Ehrburger-Dolle, F.; Morfin, I.; Bley, F.; Aguilar De Armas, M. R.; López Donaire, M. L.; San Roman, J.; Bölgen, N.; Pişkin, E.; Ziane, O.; et al. SAXS Investigation of the Effect of Temperature on the Multiscale Structure of a Macroporous Poly(N-Isopropylacrylamide) Gel. Macromolecules 2010, 43 (4), 2009–2017.

(5) Ryu, J.; Ko, J.; Lee, H.; Shin, T. G.; Sohn, D. Structural Response of Imogolite-Poly(Acrylic Acid) Hydrogel under Deformation. Macromolecules 2016, 49 (5), 1873–1881.

(6) Jaspers, M.; Pape, A. C. H.; Voets, I. K.; Rowan, A. E.; Portale, G.; Kouwer, P. H. J. Bundle Formation in Biomimetic Hydrogels. Biomacromolecules 2016, 17 (8), 2642–2649.

(7) Tominaga, T.; Tirumala, V. R.; Lin, E. K.; Gong, J. P.; Furukawa, H.; Osada, Y.; Wu, W. li. The Molecular Origin of Enhanced Toughness in Double-Network Hydrogels: A Neutron Scattering Study. Polymer 2007, 48 (26), 7449–7454.

(8) Salamon, K.; Aumiler, D.; Pabst, G.; Vuletić, T. Probing the Mesh Formed by the Semirigid Polyelectrolytes. Macromolecules 2013, 46 (3), 1107–1118.

(9) Marciel, A. B.; Srivastava, S.; Tirrell, M. V. Structure and Rheology of Polyelectrolyte Complex Coacervates. Soft Matter 2018, 14 (13), 2454–2464.

(10) Huang, M.; Furukawa, H.; Tanaka, Y.; Nakajima, T.; Osada, Y.; Gong, J. P. Importance of Entanglement between First and Second Components in High-Strength Double Network Gels. Macromolecules 2007, 40 (18), 6658–6664.

(11) Na, Y. H.; Kurokawa, T.; Katsuyama, Y.; Tsukeshiba, H.; Gong, J. P.; Osada, Y.; Okabe, S.; Karino, T.; Shibayama, M. Structural Characteristics of Double Network Gels with Extremely High Mechanical Strength. Macromolecules 2004, 37 (14), 5370–5374.

(12) Tsukeshiba, H.; Huang, M.; Na, Y. H.; Kurokawa, T.; Kuwabara, R.; Tanaka, Y.; Furukawa, H.; Osada, Y.; Gong, J. P. Effect of Polymer Entanglement on the Toughening of Double Network Hydrogels. Journal of Physical Chemistry B 2005, 109 (34), 16304–16309.

(13) Thünemann, A. F.; Ruland, W. Microvoids in Polyacrylonitrile Fibers: A Small-Angle X-Ray Scattering Study. Macromolecules 2000, 33 (5), 1848–1852.

(14) Keum, J. K.; Zuo, F.; Hsiao, B. S. Formation and Stability of Shear-Induced Shish-Kebab Structure in Highly Entangled Melts of UHMWPE/HDPE Blends. Macromolecules 2008, 41 (13), 4766–4776.

(15) Cui, K.; Meng, L.; Tian, N.; Zhou, W.; Liu, Y.; Wang, Z.; He, J.; Li, L. Self-Acceleration of Nucleation and Formation of Shish in Extension-Induced Crystallization with Strain beyond Fracture. Macromolecules 2012, 45 (13), 5477–5486.

(16) Kawai, T.; Soeno, S.; Kuroda, S. ichi; Koido, S.; Nemoto, T.; Tamada, M. Deformation Induced Void Formation and Growth in β Nucleated Isotactic Polypropylene. Polymer 2019, 178 (June), 121523.

(17) Mai, T. T.; Matsuda, T.; Nakajima, T.; Gong, J. P.; Urayama, K. Damage Cross-Effect and Anisotropy in Tough Double Network Hydrogels Revealed by Biaxial Stretching. Soft Matter 2019, 15 (18), 3719–3722.

(18) Webber, R. E.; Creton, C.; Brown, H. R.; Gong, J. P. Large Strain Hysteresis and

Mullins Effect of Tough Double-Network Hydrogels. Macromolecules 2007, 40 (8), 2919–2927.

(19) Gong, J. P. Why Are Double Network Hydrogels so Tough? Soft Matter 2010, 6 (12), 2583–2590.

(20) Na, Y. H.; Tanaka, Y.; Kawauchi, Y.; Furukawa, H.; Sumiyoshi, T.; Gong, J. P.; Osada, Y. Necking Phenomenon of Double-Network Gels. Macromolecules 2006, 39 (14), 4641–4645.

(21) Nakajima, T.; Kurokawa, T.; Ahmed, S.; Wu, W. L.; Gong, J. P. Characterization of Internal Fracture Process of Double Network Hydrogels under Uniaxial Elongation. Soft Matter 2013, 9 (6), 1955–1966.

(22) Fukao, K.; Nonoyama, T.; Kiyama, R.; Furusawa, K.; Kurokawa, T.; Nakajima, T.; Gong, J. P. Anisotropic Growth of Hydroxyapatite in Stretched Double Network Hydrogel. ACS Nano 2017, 11 (12), 12103–12110.

(23) Guo, H.; Hong, W.; Kurokawa, T.; Matsuda, T.; Wu, Z. L.; Nakajima, T.; Takahata, M.; Sun, T.; Rao, P.; Gong, J. P. Internal Damage Evolution in Double-Network Hydrogels Studied by Microelectrode Technique. Macromolecules 2019, 52 (18), 7114–7122.

(24) Nakajima, T.; Fukuda, Y.; Kurokawa, T.; Sakai, T.; Chung, U. Il; Gong, J. P. Synthesis and Fracture Process Analysis of Double Network Hydrogels with a Well-Defined First Network. ACS Macro Letters 2013, 2 (6), 518–521.

(25) Matsuda, T.; Nakajima, T.; Fukuda, Y.; Hong, W.; Sakai, T.; Kurokawa, T.; Chung, U. Il; Gong, J. P. Yielding Criteria of Double Network Hydrogels.

Macromolecules 2016, 49 (5), 1865–1872.

CHAPTER 4: Anisotropic HAp growth in stretched DN gels [1]

4.1 Introduction

In chapter 4, to apply the change in the internal structure of DN gels, which revealed in chapter 3, to novel functional material development, I worked on developing the anisotropic HAp/DN hybrid materials imitating the forming process of bone tissue. The biological hard tissues such as bone have acquired excellent mechanical properties to support self-standing of body and to protect important organs.[2,3] The hard tissues are composed of organic biomacromolecules and mineral, and their anisotropic structure play important roles to achieve such mechanical performances.[2,4,5] During a biosynthesis process of construction of hard tissues called as biomineralization, biomacromolecules, such as collagen, firstly self-assemble to strictly regulated network structure, and then nucleation of mineral occurs at the anionic functional groups of the biopolymer network.[6] Finally, the embryos grow into anisotropic minerals in the space of the self-assembled organic template.[7] From the detailed observation of osteogenesis, the nucleation of hydroxyapatite (HAp) occurs at the nano-scale gaps of self-assembled collagen fibrils, and c-axis of HAp orientates along the longitudinal direction of collagen fibrils.[3,8–11] The nano/microscopic orientation contributes macroscopic mechanical anisotropy of bone tissues. Such anisotropic crystal growth regulated by the anisotropic organic template has potential to produce fine anisotropic organic/inorganic hybrid materials.[12]

PAMPS/PAAm DN gels have shown excellent biomechanical performances as artificial articular cartilages and as scaffolds for inducing spontaneous cartilage regeneration in vivo.[13,14] For these applications, fixation of the DN gels on bones is necessary. However, given its high water-content (~90 wt%), the DN gels cannot be firmly fixed onto bones by any glues. Recently, our group have developed soft biomaterials, called as "soft ceramics", from combination of DN gels and bioceramics HAp.[15,16] To overcome the problem about the fixation of the DN gels on bones, HAp nano-particles in the surface layer of DN gels was induced at the condition of homogeneous nucleation using high concentration solutions of the mineralization. The surface modification of the osteo-inert DN gel imparted robust bonding ability of DN hydrogels to bone tissues in vivo owing to osteogenesis penetration into the gel matrix. From these previous reports, DN gels were found to be excellent matrix for HAp mineralization, because a great advantage of DN gels in comparison to conventional polyelectrolyte gels is their size stability in high concentration solutions of mineralization despite with possessing anionic functional groups. As a result, the HAp/DN gels acquire HAp characteristics such as osteoconduction while preserving original flexibility and strength of the DN gel matrix.

In this chapter, I adopted a DN hydrogel consisted of PAMPS as the first network and PAAm as the second network. Taking the advantage of DN gel's the high stretchable capacity, our strategy to induce anisotropic HAp growth was to perform the heterogeneous HAp nucleation and mineralization in the highly stretched PAMPS network, which possesses the sulfonic functional group, of the DN gels. It is well-known that sulfonic groups can capture calcium ion and induce heterogeneous HAp nucleation and crystallization.[17,18] I expected that the macroscopic stretching of DN gels can induce nanoscale anisotropic PAMPS network distribution for reactive field of mineralization.[19-22] The DN gel was stretched at various stretch ratios λ to change the microscopic spatial distribution of PAMPS network, and HAp mineralization was performed in the stretched DN hydrogels at mineralizing solution of relatively low concentration for heterogeneous nucleation. The relation between stretch ratio of the DN gels and the anisotropy of mineral growth is quantitatively studied by the X-ray diffraction technique. The mechanism for the anisotropic growth is also discussed.

,

4.2 Experiments

4.2.1 Materials

2-Acrylamido-2-methyl propanesulphonic acid (AMPS) was provided by Toagosei Co. Ltd. (Japan). Acrylamide (AAm), dimethylacrylamide (DMAAm), *N,N'*-methylenebisacrylamide (MBAA), 2-oxoglutaric acid (α-keto), calcium chloride ($CaCl_2$) and dipotassium phosphate (K_2HPO_4) were purchased from Wako Pure Chemical Industries, Ltd. (Japan). Natural bone tissues derived from Japanese white rabbit and pig were used as reference specimens on X-ray diffraction analysis. Femoral and tibial bones for rabbit and tibial bone for pig were harvested, and inner cancellous region was removed from outer cortical region. The cortical bone was shaped into slender rectangle to be planar substrate. Finally, thickness was reduced to around 0.05 mm by filing.

4.2.2 Synthesis of PAMPS/PAAm DN gels

The PAMPS/PAAm DN gel was synthesized using above-described methods (**section 3.2.4**). PAMPS gel was firstly synthesized by radical polymerization from aqueous solution, containing 1 M AMPS, 2 mol% MBAA and 0.1 mol% α-keto. The solution was injected into a mold (0.5 mm-thick silicone rubber). The PAMPS gel obtained as first network was then immersed in an aqueous solution containing 2 M AAm, 0.02 mol% MBAA, and 0.01 mol% α-keto for 1 day until reaching equilibrium and polymerized again by irradiating with UV light for 8 h under argon gas. The obtained PAMPS/PAAm DN gel was immersed in distilled water for 1 week to remove any unreacted chemicals. For TEM measurement, the PAMPS/PDMAAm DN gel (0.02 mol% MBAA for second polymerization) was synthesized by the same protocol.

PAAm SN gel as reference sample was synthesized by radical polymerization from aqueous solution using same procedure of **section 3.2.3**. This solution contained 2 M AAm, 0.02 mol% MBAA, and 0.01 mol% α-keto.

4.2.3 HAp mineralization in stretched DN gel

First, dumbbell shaped DN gel (1.6 mm thickness, 20 mm gauge length and 20 mm width in test region) was fixed under various stretch ratios (λ = 1, 2, 3 and 4) by a tailor-made stretching device. The mineralization was performed at heterogenous nucleation condition. The DN gel was immersed in large amount of 50 mM $CaCl_2$ aq at room temperature for 5 h (pH 9.0). The condition for the formation of HAp is the most suitable in pH 8-9 solution.[23] The gel was then washed by distilled water to remove excess calcium ions at gel surface. The DN gel was immersed in 30 mM K_2HPO_4 aq for 5 h, and washed. This alternative immersing process was repeated for 10 cycles to mineralize calcium phosphate. After the alternative immersing, the DN gels were immersed in 50 mM $CaCl_2$ aqueous solution (pH 9) at room temperature over 1 day to ripen the mineralized amorphous calcium phosphate (ACP) to HAp. The obtained HAp/DN gel was stored in distilled water.

4.2.4 Thermogravimetric/differential thermal analysis (TG/DTA)

The compositions of three kinds of components in HAp/DN hydrogels, water, polymer, and mineral, were evaluated using a thermogravimetric analyser (TG820 Thermo plus EVO, Rigaku). The HAp/DN hydrogel (several dozen milligrams) was loaded in a platinum open pan, and the weight and differential thermal (DT) were measured from 30 to 600 °C at a heating rate of 10 °C/min, respectively. The ratio by weight of water was determined by the total weight change from 30 °C to a temperature indicating that the DT was 0 (around 150–200 °C). The ratio by weight of mineral was determined from the final residue at 600 °C, and the polymer fraction was determined by the difference between the original weight and the sum of the water and mineral weights.

4.2.5 Identification of crystal phase of mineralized calcium phosphate by X-ray diffraction (XRD)

The crystal phase of mineralized calcium phosphate was evaluated by XRD spectrometer (Ultima IV, Rigaku, Japan). The extraction wavelength and output power of X-ray generated by the Cu cube were 1.5406 Å and 0.8 kW (40 kV and 20 mA), respectively. The range of diffraction angle 2θ was from 10° to 60° at a scanning rate of 3 °/min.

4.2.6 Attenuated total reflection Fourier-transform infrared spectroscopy (ATR-IR)

Interaction between HAp and sulfonic group of PAMPS/PAAm DN gel was evaluated by

ATR-IR (IRT-3000N, Jasco, Japan). HAp/DN gels were fully contacted with a zinc selenide prism and were measured from 1400 to 1900 cm^{-1}. The calculated number was 128.

4.2.7 Wide angle x-ray diffraction (WAXD) measurement

The anisotropies of HAp were evaluated by high-brightness synchrotron X-ray facility of beam line BL40B2 in SPring-8 (Hyogo, Japan). For WAXD to evaluate HAp nano-crystal, the extraction wavelength of synchrotron X-ray generated by deflection electric magnet was 0.708 Å (17.5 keV in energy). The camera length, the distance between sample and imaging plate detector, was 0.29 m. The irradiation time was 60 s to obtain 2D scattering images. The elongation axis was set in parallel to the equatorial direction.

4.2.8 Analysis of anisotropy of mineralized HA

To evaluate anisotropy of mineralized HAp in stretched DN gel matrix, I calculated orientation degree from 2D WAXD images. The intensities of water profile were much higher than those of HAp in the raw 2D WAXD images. To isolate HAp diffraction profile, I subtracted the 2D image of pristine DN gel from that of HAp/DN gel by image calculator processing on Image J (v1.49) software. Next, azimuthal angle distributions of HAp were calculated from the isolated 2D profile by using Fit_2D (v12.077) software. I defined azimuthal angle (φ) starting from equatorial direction anticlockwisely in 2D images. I integrated the intensities in φ = -15 ° ~ 15 °, and φ = 75 ° ~ 105 ° for outputting parallel and perpendicular 1D profiles to the stretching direction, respectively. Finally, orientation degree was calculated according to Herrmann’s orientation function, S, as follows.

- $S = \frac{3\langle\cos^2\varphi\rangle-1}{2}\ (-0.5 \leq S \leq 1),$

$$\langle\cos^2\varphi\rangle = \frac{\int_{\varphi_1}^{\varphi_2} I(\varphi, 002)\cos^2\varphi\sin\varphi\, d\varphi}{\int_{\varphi_1}^{\varphi_2} I(\varphi, 002)\sin\varphi\, d\varphi}$$

where $I(\varphi,\ 002)$ was intensity of (002) plane. For calculation of S, range of φ was from 0 ° to 90 °. Here, $-0.5 \leq S < 0$, $S = 0$ and $0 < S \leq 1$ indicated parallel, random and perpendicular orientations, respectively. -0.5 and 1 mean perfectly parallel and perpendicular orientations, respectively.

Deconvolution of dense peak around 32° was performed using the mixed Gaussian-Lorentzian function (pseudo-Voigt function) as follow.[24] The Gauss/Lorentz ratio was 1/99.

$$V(x) = (1-\eta)\times\frac{2I}{H}\left(\frac{\ln 2}{\pi}\right)^{\frac{1}{2}} exp\left\{-4\,ln\,2\left(\frac{(x-x_0)}{H}\right)^2\right\} + \eta\times\frac{2I}{\pi H}\left\{1+\left(\frac{2(x-x_0)}{H}\right)^{-1}\right\}$$

To estimate the angular spread of HAp (002) plane, I obtained azimuthal angle plots of HAp (002) plane of all samples including bone tissues by using Fit_2D (v12.077) software. And then I fitted Lorentzian function for obtained azimuthal angle plots by using origin (v94J) software to calculate the full width half maximum (FWHM) of each azimuthal angle plot.

4.2.9 Analysis of reversibility of mineralized HAp

To evaluate the effect of stretching and unstretching of DN hydrogels on the orientation of mineralized HAp, I measured the crystalline structure of HAp/DN gels at relaxed state by using WAXD. Firstly, HAp was mineralized in DN hydrogels at various stretch ratios (λ =2, 3 and 4). Then the stretching force exerted on the HAp/DN hydrogels) were removed, and the samples that exhibited residual deformation ratio $\lambda_{residual}$ = 1.3, 1.6, 2.1 at relaxed state for λ =2, 3 and 4, respectively, were measured by WAXD. As a comparison, the HAp/DN hydrogel mineralized at unstretched state (λ = 1) was elongated to λ = 2, 3 and 4 and WAXD was also measured to evaluate the effect of post elongation on the orientation of mineralized HAp. Then I calculated Herrmann's orientation function, S to compare the orientation degree between these samples.

4.2.10 Field emission transmittance electron microscopy (TEM)

The morphology of HAp in the stretched DN gel was evaluated by FE-TEM (JEM-2100F, JEOL, Japan). PAMPS/PDMAAm DN matrix was applied for the observation because PAMPS/PAAm DN gel formed phase separation during solvent exchanging in sample preparation. The samples were fixed by plastic holders to keep stretching and were lyophilized by liquid nitrogen. The water within the hydrogel was exchanged with acrylic resin (London Resin white) in a chamber of an automatic freeze substitution system (EM AFS2, Leica Microsystems, Germany). Sections (100 nm thick) of the resin-cured samples were cut by an ultra-microtome with diamond knife (EM UC7i, Leica Microsystems, Germany) and placed on a copper mesh TEM grid. The acceleration voltage of the electron gun for observation was 200 kV. Selected area two-dimensional fast Fourier transformation (SA-2DFFT) of atomic images in high magnification images was carried out by image J (v1.49).

4.2.11 Comparison of anisotropy between HAp/DN gel and HAp/SN gel

The anisotropies of HAp were evaluated by high-brightness synchrotron X-ray facility of beam line BL05XU in SPring-8 (Hyogo, Japan). For WAXD to evaluate HAp nano-crystal, the extraction wavelength of synchrotron X-ray generated by deflection electric magnet was 1 Å (12.4 keV in energy). The camera length, the distance between sample and flat panel detector, was 0.066 m. The irradiation time was 400 ms to obtain 2D scattering images. The elongation axis was set in parallel to the horizontal direction.

To compare the anisotropy of mineralized HAp between SN and DN gel, I calculated the ratio of azimuthal angle intensities at φ=0 and 90 for (002) plane.

4.2.12 Tensile test of stretched HAp/DN gel

To evaluate the mechanical property of HAp/DN gel mineralized at stretching state, I carried out tensile test. Firstly, non-stretched (λ = 1) and stretched (λ = 4) DN gel was mineralized. After relaxing of stretched DN gel mineralized with HAp, the sample, 1.7 mm-thick in test region, was cut into two dumbbell shapes (6 mm gauge length and 2 mm width), with long axe parallel and perpendicular to stretching direction of DN gel matrix, respectively. And then, I performed uniaxial tensile test at 100 mm/min by using tensilon RTC-1150A (ORIENTEC Corporation, Japan). To consider the effect of anisotropy of stretched DN gel, I also performed the tensile test on pre-stretched DN gel (λ = 4) immersing in 50 mM calcium chloride solution for the same time of HAp mineralization.

4.3 Results & discussion

4.3.1 Characteristic properties of HAp/DN gels

The PAMPS/PAAm DN gel was synthesized by two-step polymerization (details are shown in **section 4.2.2**), and its tensile stress- stretch ratio (σ–λ) curve showed linear elastic region at small λ, yielding at $\lambda = 3.8$, and strain hardening far beyond the necking (**Figure 4-1**). Previous reports and results in chapter 4 explained that the necking behavior occurs due to the fracture percolation of the fully stretched first polymer network under stretching.[25] Beyond the necking point, the anisotropy of the first PAMPS network less increases with the increase of stretch ratio λ. According to the tensile profile, I selected λ = 1, 2, 3 and 4 for the HAp mineralization. Heterogeneously nucleated HAp mineralization was carried out by alternative soaking method.[26,27] A piece of

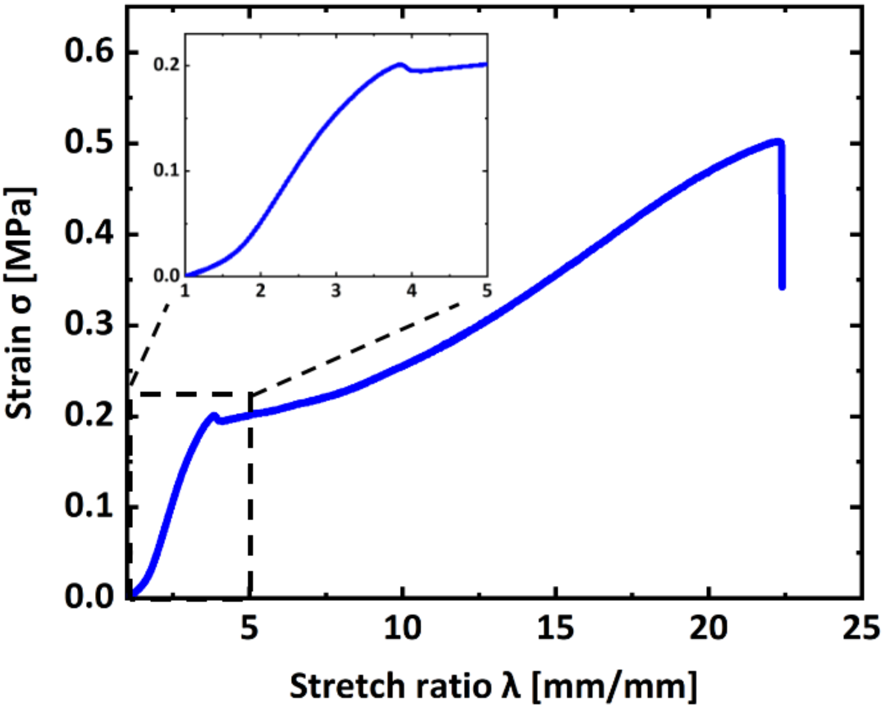

Figure 4-1. Tensile stress-elongation ratio (σ-λ) curve of pristine DN hydrogel. The inset magnification exhibits that yielding point is λ = 3.8

PAMPS/PAAm DN gel was stretched by a tailor-made stretching device at an stretch ratio λ to induce the anisotropy of PAMPS network distribution, and then was immersed in calcium chloride ($CaCl_2$) aqueous solution and dipotassium hydrogen phosphate (K_2HPO_4) aqueous solution, alternatively. The process was repeated for 10 cycles to obtain the HAp mineralized samples (details are shown in **section 4.2.3**).

Figure 4-2 showed the appearance of pristine DN gel and HAp mineralized DN gel fixed by the stretching device. The transparent DN gels became opaque white and did not show any cracks caused by structure mismatch during mineralization. At the same mineralization condition, the mineral contents slightly decreased with increase of stretch ratio, measured by thermogravimetrical / differential thermal analysis (TG/DTA) (**Figure 4-3**, **Table 4-1**). X-ray diffraction (XRD) revealed that weak characteristics peaks assigned as HAp crystal appeared in all mineralized samples (**Figure 4-4(a)**).[28,29] The interaction between HAp and sulfonic functional group of the PAMPS network was

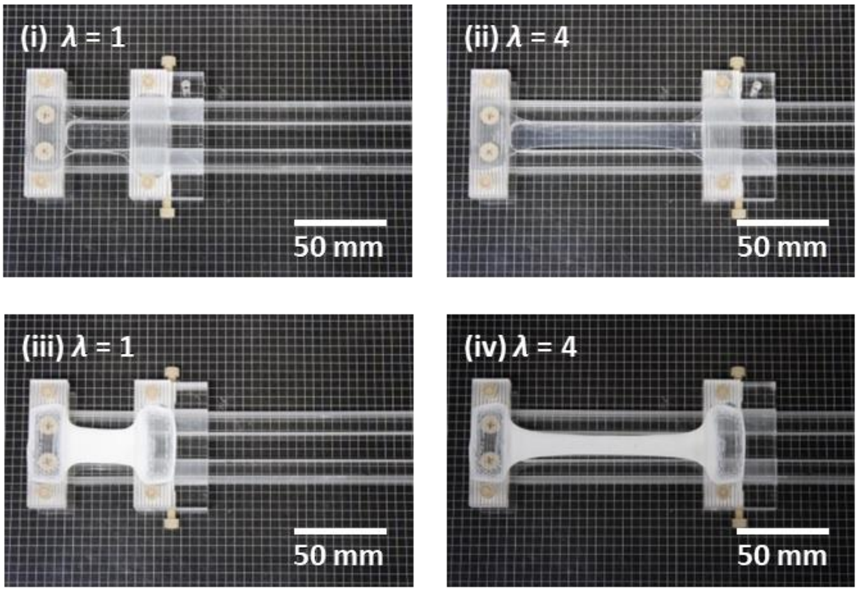

Figure 4-2. Appearances of pristine DN gel at different stretching ratio λ ((i), (ii)), and HAp/DN gel mineralized at different stretching ratio λ ((iii), (iv)).

evaluated by attenuated total reflection IR spectroscopy (ATR-IR). The peak at 1190 cm^{-1} assigned as S=O stretching mode showed slight red shifting after mineralization, indicating the weak interaction between HAp and sulfonic group of PAMPS network (**Figure 4-4(b,c)**).[30,31] Therefore, HAp embryos were formed in the vicinity of the sulfonic groups in the PAMPS/PAAm DN gel and then grew to microcrystals.

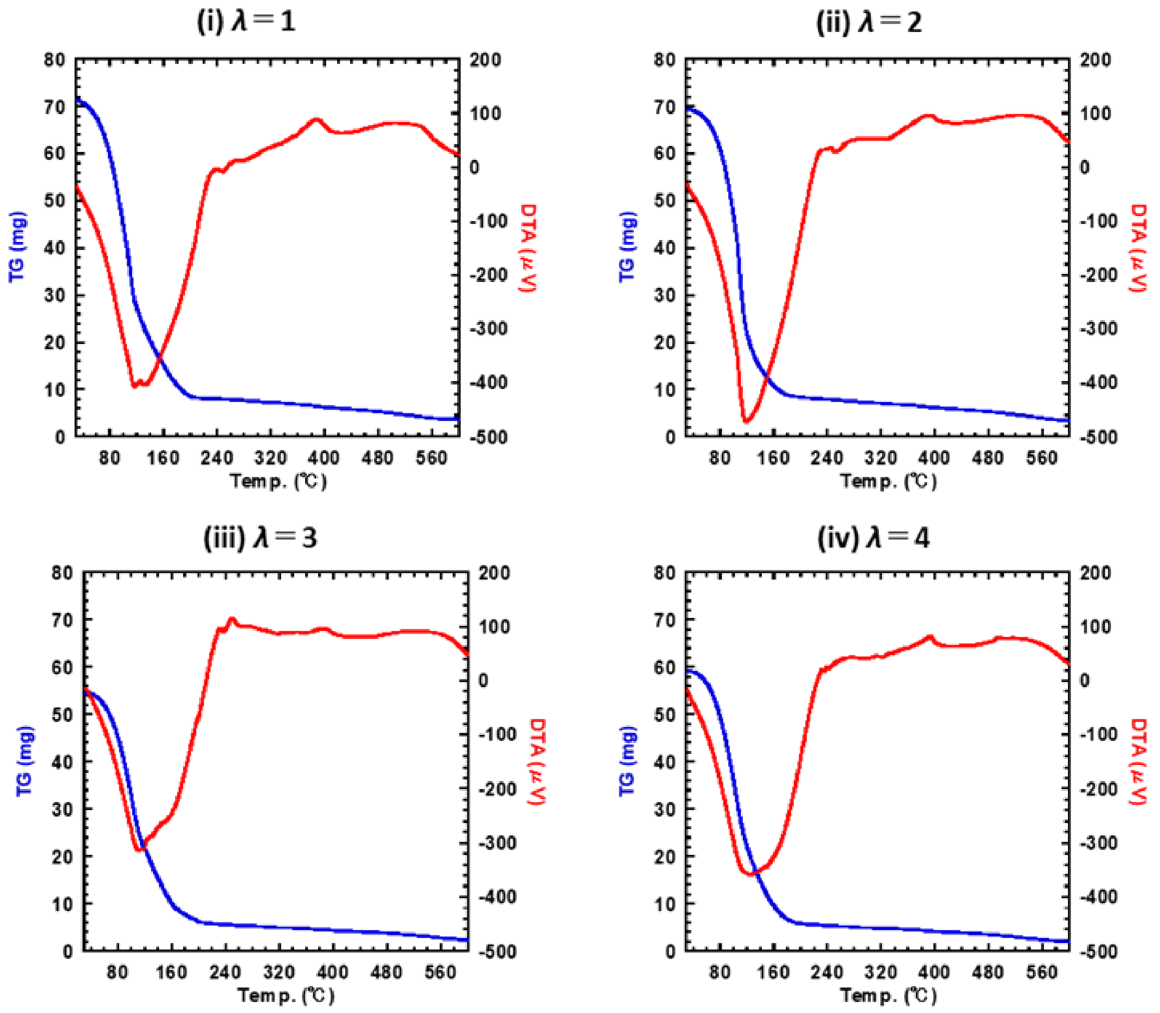
(i) $\lambda = 1$

(ii) $\lambda = 2$

(iii) $\lambda = 3$

(iv) $\lambda = 4$

Figure 4-3. TG/DTA profiles to calculate weight fractions of water, polymer and HAp of HAp/DN gels mineralized at various elongation ratios λ. (i) λ = 1, (ii) λ = 2, (iii) λ = 3, (iv) λ = 4.

Table 4-1. Weight fraction of water, polymer and HAp of HAp/DN gels mineralized at various stretch ratios λ.

	Weight fraction (wt%)		
stretch ratio λ	water	polymer	HAp
1	88.78	6.04	5.19
2	88.64	6.48	4.88
3	89.47	6.18	4.35
4	90.70	5.79	3.51

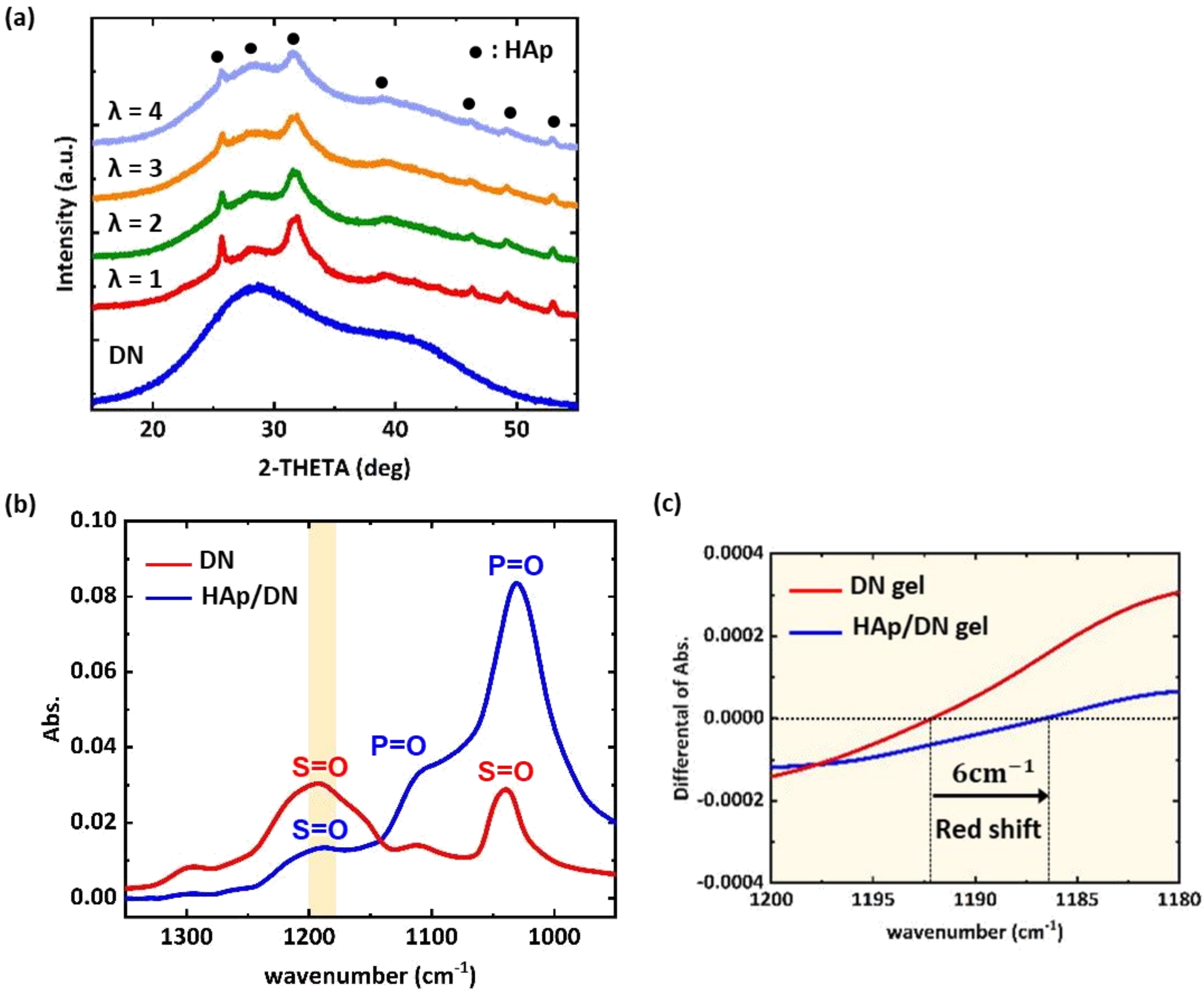

Figure 4-4. (a) X-ray diffraction patterns of non-stretched pristine DN gel and HAp/DN gels mineralized at different stretch ratio λ. (b) ATR-IR spectra of pristine DN gel and HAp/DN gel (λ = 1). (c) The differentials of ATR-IR spectra on yellow part to obviously show the peak shifting.

4.3.2 Anisotropy of mineralized HAp in stretched DN gels

To evaluate the effect of stretching of DN gel on HAp mineralization, I measured 2D wide-angle X-ray diffraction (WAXD) of the mineralized HAp in stretched DN gel by using high-brightness synchrotron X-ray facility (BL40B2) in SPring-8. Stretching direction of DN gel was set in parallel to equatorial axis (**Figure 4-5**). **Figure 4-6(a)** showed the 2D WAXD images of HAp crystal mineralized in stretched DN gel. The isotropic Debye-Scherrer rings assigned as (002) and (004) of HAp were observed in λ = 1, and the rings changed to the crescent arcs whose parallel intensity increased with increase of stretch ratio (λ = 2, 3, 4). I furthermore plotted 1D profiles from the 2D images to isolate perpendicular and parallel profiles (**Figure 4-6(b)**). The peak intensities of (002) and (004) became higher and lower for parallel and perpendicular directions, respectively, compared with those of λ = 1. Also, the dense peak around 32° showed significant

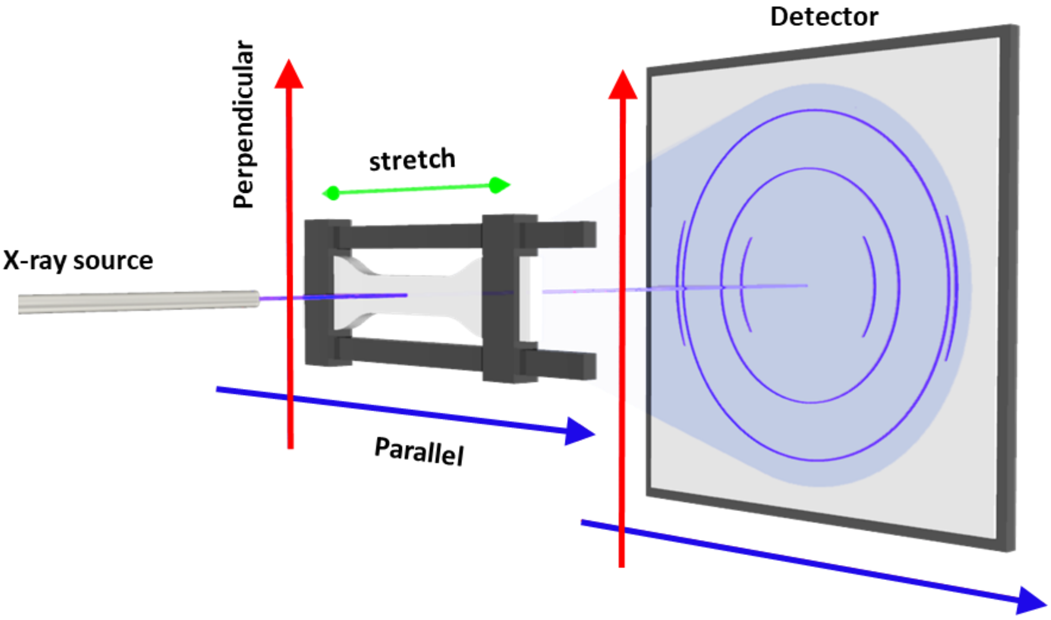

Figure 4-5. Schematic image of WAXD measurement geometry.

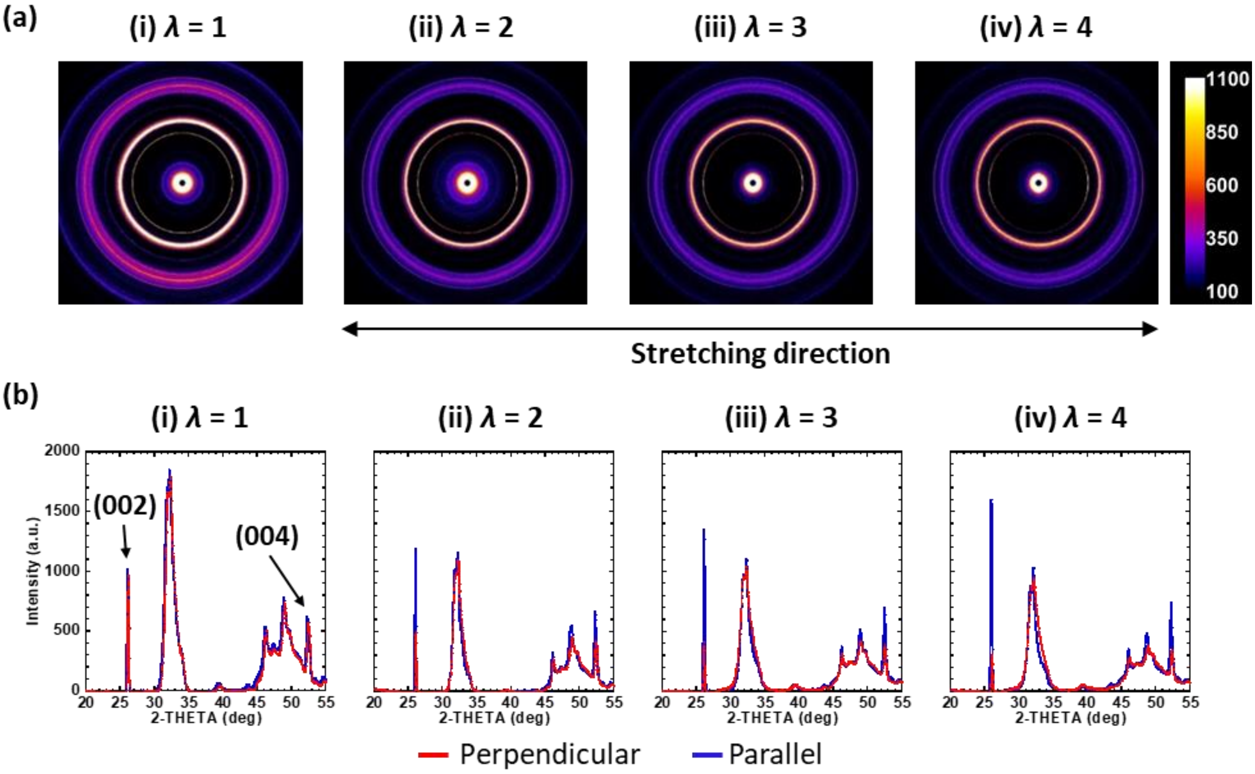

Figure 4-6. (a) Wide angle X-ray 2D diffraction images of HAp/DN gels mineralized in elongated state of DN gelz at (i) $\lambda = 1$, (ii) $\lambda = 2$, (iii) $\lambda = 3$ and (iv) $\lambda = 4$. (b) Perpendicular (red) and parallel (blue) 1D profiles isolated from (a); (i) $\lambda = 1$, (ii) $\lambda = 2$, (iii) $\lambda = 3$, (iv) $\lambda = 4$.

difference between perpendicular and parallel directions in $\lambda = 2, 3, 4$. Deconvolution of the dense peak ($\lambda = 4$) to typical XRD peaks of HAp revealed the larger (112) and lower (300) peaks for the parallel direction compared with those of the perpendicular direction (**Figure 4-7**). From these diffraction results, I can estimate that *c*-axis of HAp aligned in parallel to the stretching direction of DN gel. The orientation degree of (002) of mineralized HAp was calculated from equation of Herrmann's orientation function, S_{HAp}.[32,33] For $\lambda = 1$, S_{HAp} was 0 indicating perfectly random orientation. On the other hand, for $\lambda = 2, 3, 4$, the value of S_{HAp} increased with increasing of stretch ratio λ ((**Figure 4-8(a)**).

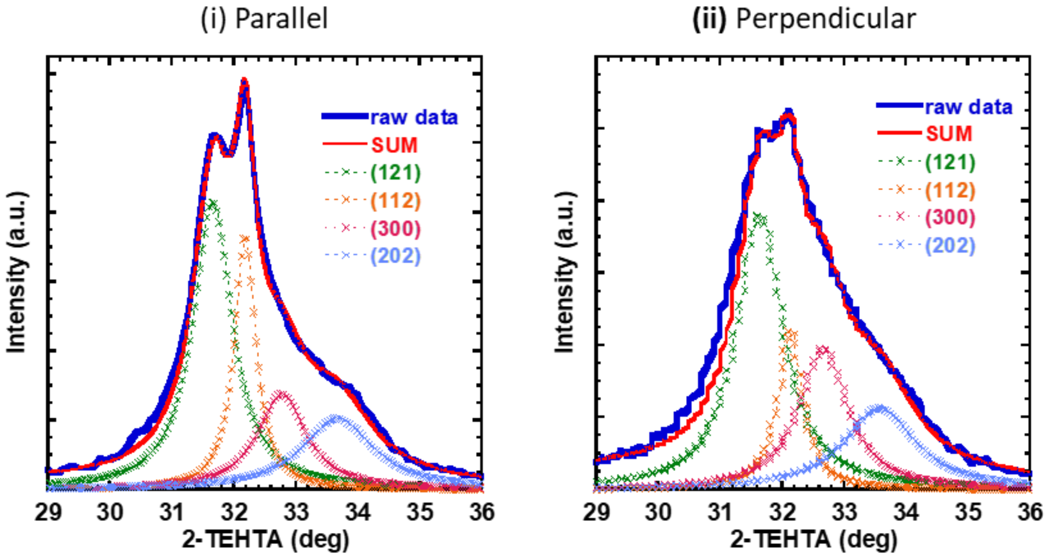

Figure 4-7. Wave separation from the dense peaks of HAp around 2-THETA = 32°of WAXD at (i) parallel and (ii) perpendicular directions.

When the DN samples mineralized in stretching state were relaxed, only a small residual stretch ratio ($\lambda_{residual}$ ~ 1.3, 1.6, 2.1 for λ = 2, 3, 4, respectively) was observed. The interesting phenomenon is that the anisotropy of the HAp structure only slightly decreased in the relaxed DN gel, after removing of the stretching, and the sample recovered to the same level of anisotropy after restretching λ' (**Figure 4-9**). **Figure 4-8(a)** showed that S_{HAp} of relaxed state for all stretch ratios only slightly decreased from that of initial stretching state λ, and S_{HAp} of restretching state λ' was almost the same as that of the initial state λ. I also found that the HAp mineralized in unstretched DN gel did not show distinct anisotropy even at elongated state λ'', which indicated the S_{HAp} is almost 0 (**Figure 4-8(b), Figure 4-10**). From these results, the initial stretching of the DN gel induces the anisotropic mineralization of HAp, and post stretching after HAp mineralization does not affect the orientation of the HAp crystalline. The above results suggest that anisotropy in PAMPS network structure before HAp mineralization determines the HAp crystal growth direction.

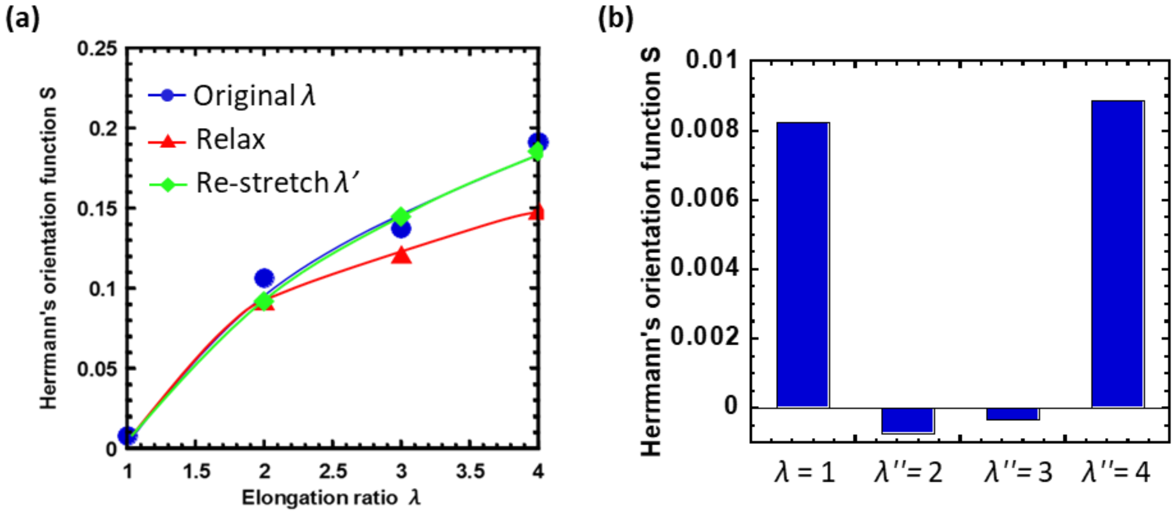

Figure 4-8. (a) Orientation degrees S of HAp for the sample mineralized at stretched state, and measured at stretched (λ), relaxed, and re-stretched (λ’) states. (b) Orientation degrees S of HAp for the sample mineralized at non-stretching state and measured at post-stretched state λ”.

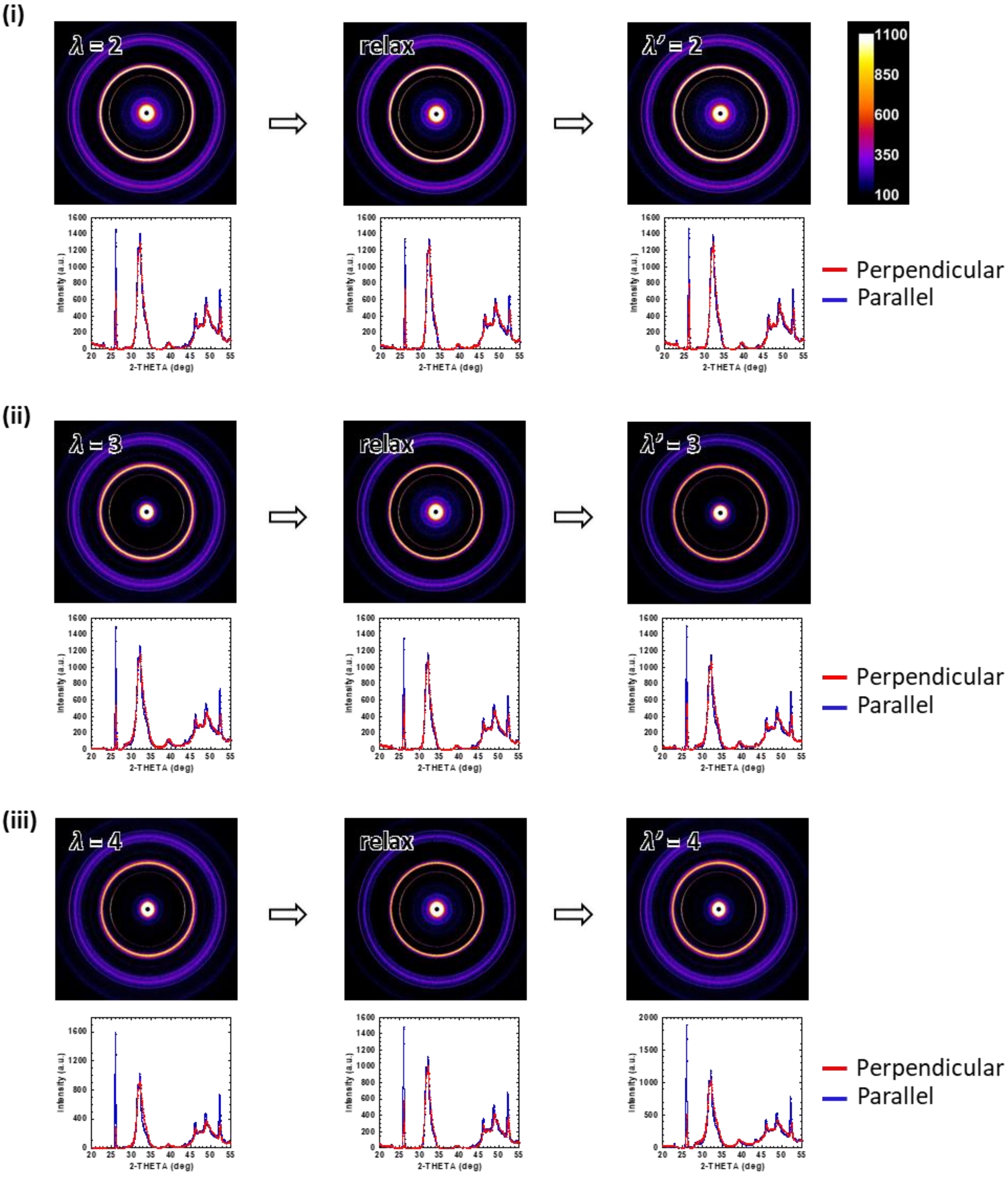

Figure 4-9. WAXD profiles of HAp/DN gels mineralized at various stretch ratios λ. The measurements were performed at the as-prepared stretching state (λ), at relaxed state ($\lambda_{residual}$), and at re-stretching state (λ'). $\lambda_{residual}$ =1.3, 1.6, 2.1 for λ = 2, 3, 4, respectively. (i) λ = 2, (ii) λ = 3, (iii) λ = 4.

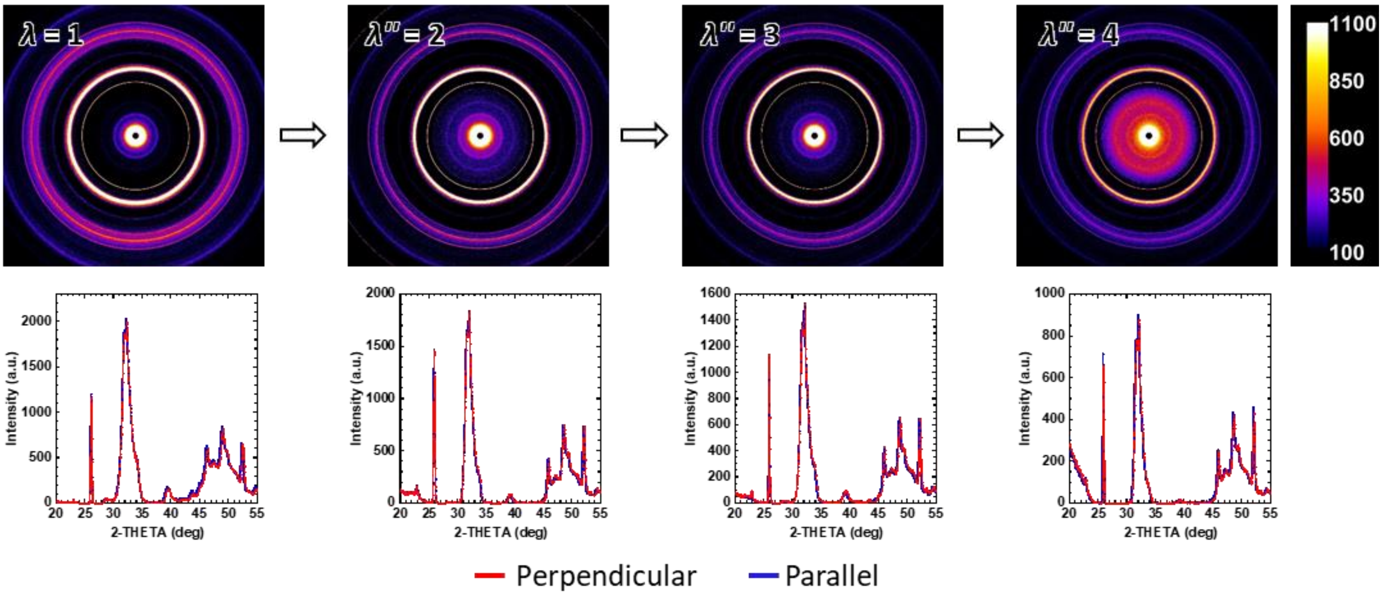

Figure 4-10. 2D and 1D WAXD profiles of HAp/DN hydrogels mineralized at unstretched state. The experiment was performed on the sample at various post-stretching state of λ” = 2, 3, 4.

4.3.3 The morphology of mineralized HAp in stretched DN gels

To understand how the anisotropic orientation of the HAp is fixed even after relaxing the DN gel to non-stretched state, the morphology of HAp crystals was observed by transmission electron microscopy (TEM) (**Figure 4-11**). Spiny polycrystalline spheres of 1 μm in diameter were observed for the sample of $\lambda = 1$. The sphere was the aggregation of many single crystal rods (~15 nm in diameter and ~230 nm in length) that aligned isotopically in radial direction. While in stretched DN gel (λ = 2, 3 4), the spiny polycrystalline became anisotropic with long axis of single crystal rods aligned

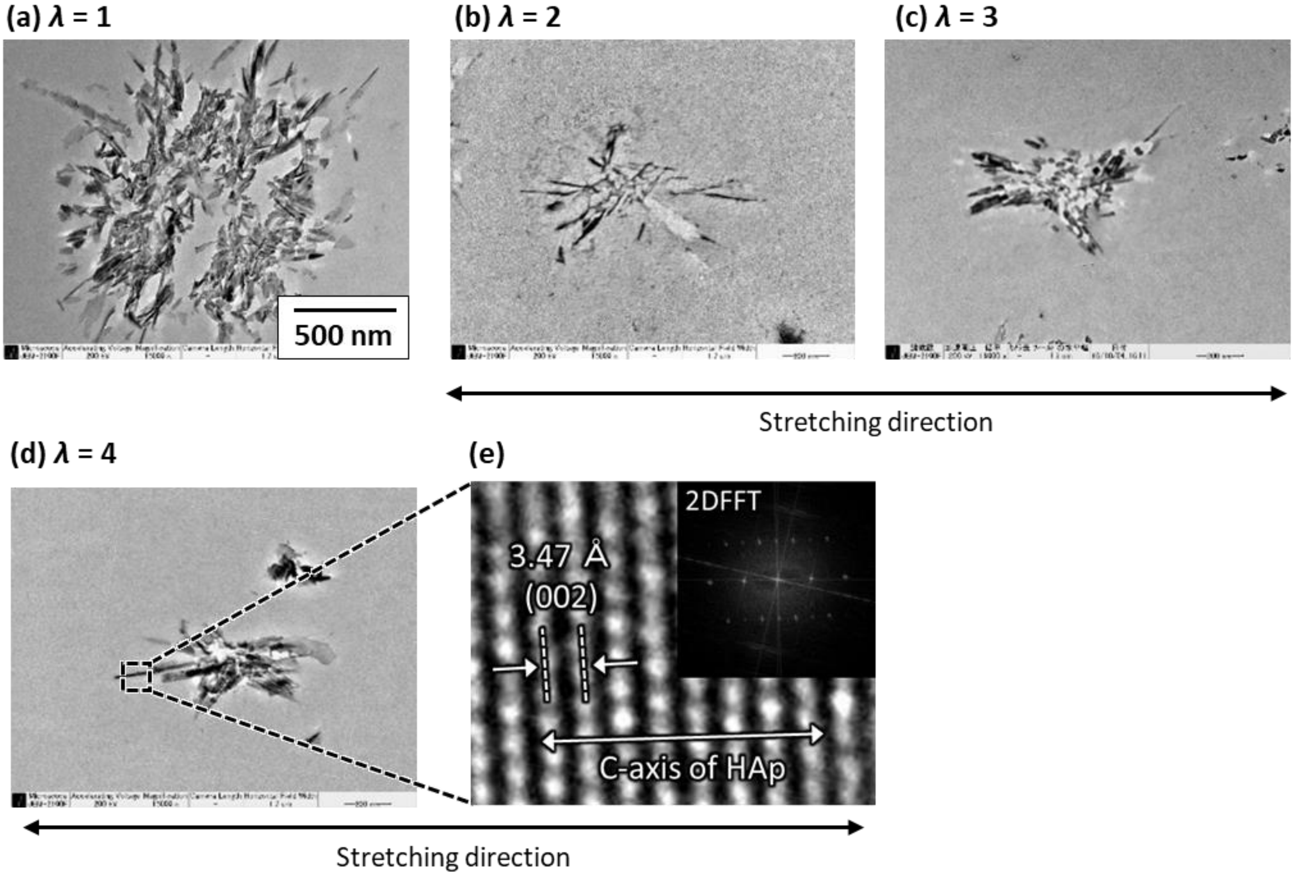

Figure 4-11. TEM images of the HAp clusters in HAp/DN gel mineralized at different elongation ratio of gel matrix; (a) λ = 1, (b) λ = 2, (c) λ = 3, (d) λ = 4. (e) is high magnified image of HAp single crystal rod in (iv). (a)-(d) have the same scale as shown in (a).

preferentially along the stretch direction. High magnification TEM image further showed that the (002) plane of the HAp lattice was perpendicular to the stretch direction. These results mean that the long axis of the single crystal rod was along the *c*-axis of HAp lattice, and the latter was aligned along the stretching direction. As the size of a HAp polycrystalline sphere (~1μm) was much larger than the mesh size of polymer network (several tens nm in maximum),[22,34] the polymer network was incorporated in the HAp sphere during crystal growth, probably at the interfaces of the single crystal rods. Accordingly, the fixation of the anisotropic orientation of the HAp even after relaxing the DN gel is due to the large structure formation of the HAp crystals.

The differences in the length scale between the mesh size of the network (~ nm) and the HAp crystals (~1 μm) suggest that it is not the molecular scale orientation of polymer strands, but a larger scale structure, is relevant for the orientation of the HAp crystals at stretching. What is this structure? According to the previous studies, the DN gel has the submicron-scaled voids of first PAMPS network.[22] Given the heterogeneous nucleation condition of the HAp mineralization adopted in this work, HAp grows in the region having PAMPS network but does not in the region without PAMPS. Thus, the crystal growth of HAp, along its *c*-axis, is regulated by the spatial distribution of PAMPS network. Due to the presence of void structure of the PAMPS network, the HAp polycrystalline only grows in the void-free region, which is isotropic in the non-stretched DN gel, resulting in the isotopic growth of HAp nano crystalline rods. In the stretched DN gel, the corresponding void free region is elongated, which restricts the growth of the HAp crystalline rods in the direction perpendicular to the stretch direction, resulting in the preferential growth of HAp along the stretching direction. This probable mechanism is illustrated in **Figure 4-12**.

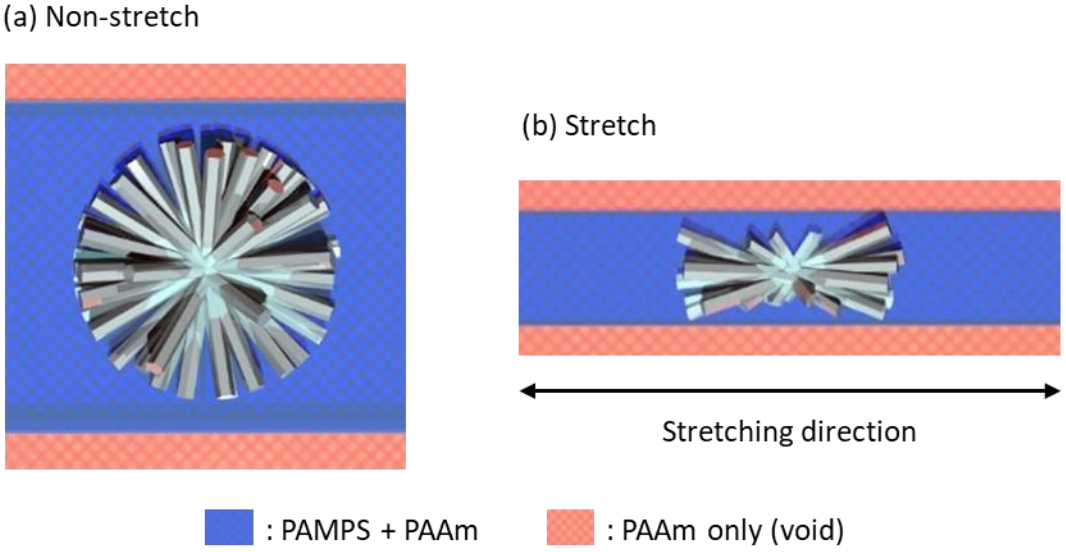

Figure 4-12. Given the heterogeneous nucleation condition of the HAp mineralization adopted in this work, HAp grows in the region having PAMPS network (blue) but does not in the region without PAMPS (pink). Thus, the crystal growth of HAp, along its c-axis, is regulated by the spatial distribution of PAMPS network. Due to the presence of void structure of the PAMPS network, the HAp polycrystalline only grows in the void-free region (blue), which is isotropic in the non-stretched DN gel, resulting in the isotopic growth of HAp single crystalline rods. In the stretched DN gel, the corresponding void free region is elongated, which restricts the growth of the HAp crystalline rods in the direction perpendicular to the stretch direction, resulting in the preferential growth of HAp along the stretching direction.

To support the argument that the anisotropy of PAMPS polymer network distribution affects HAp crystallization, I compared HAp orientation in stretched PAMPS/PAAm DN gel with that in stretched PAAm SN gel. HAp is mineralized in PAAm SN gels by homogeneous nucleation mechanism. 2D diffraction images clearly showed that HAp nanocrystals were not oriented even in the stretched PAAm SN gel in $\lambda = 4$ (**Figure 4-13, Table 4-2**). The evidence strongly supports that the orientation of mineralized HAp is induced by presence and distribution of PAMPS polymer network in DN gel.

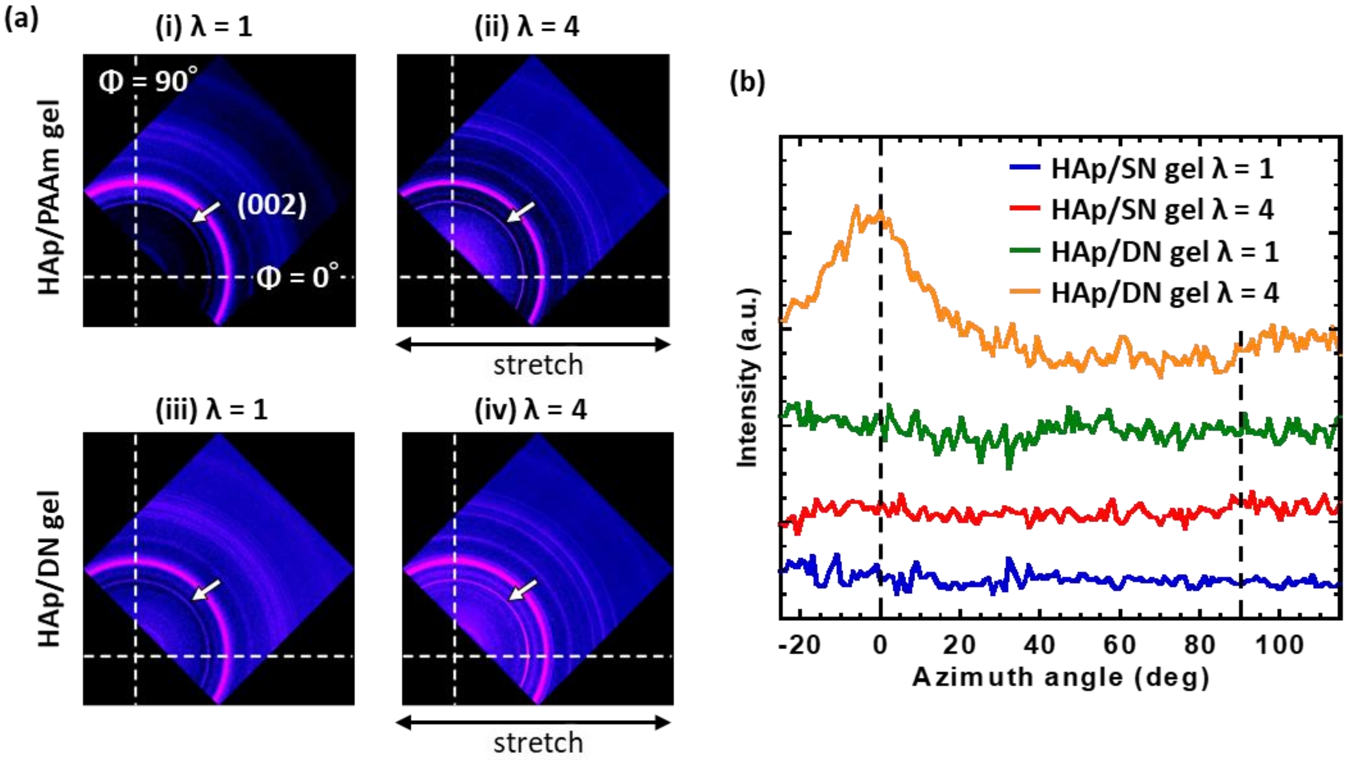

Figure 4-13. (a) Wide angle X-ray 2D diffraction images of HAp/DN and HAp/SN gels mineralized at different elongation. (i) λ = 1 and (ii) λ =4 for HAp/SN and (iii) λ = 1 and (iv) λ = 4 for HAp/DN gel. Arrows indicate the profile of (002) plane of HAp for equatorial direction to elongating direction. (b) Comparison of azimuthal angle plots of HAp (002) plane.

Table 4-2. Ratio of azimuthal angle intensities at φ = 0 and 90 for (002) plane of HAp. φ = 0 defined by the stretching direction.

		I (φ=0) / I (φ=90)
HAp/SN gel	$\lambda = 1$	1.10
	$\lambda = 4$	0.95
HAp/DN gel	$\lambda = 1$	1.04
	$\lambda = 4$	1.49

4.3.4 Comparison the anisotropy with natural bone tissues

To compare the orientation of synthetic HAp in stretched DN gel with biomineralized HAp of natural bone tissues, I also evaluated HAp anisotropy of cortical region of femoral (rabbit) and tibial bones (rabbit and pig). The long axis of bones was parallel to the equatorial direction. Obvious orientations of bone HAp were observed in WAXD profiles (**Figure 4-14(a)**). The calculated orientation degree S_{bone} was comparable to that of mineralized HAp in stretched DN gel. To estimate the angular spread of HAp (002) plane, I obtained azimuthal angle plots of HAp (002) plane of all samples including bone tissues (**Figure 4-14(b)**). And then I fitted Lorentzian function for obtained azimuthal angle plots to calculate the full width half maximum (FWHM) of each azimuthal angle plot (**Table 4-3**). In this result, the value of FWHM of mineralized HAp in stretched DN hydrogels is relatively smaller than that of HAp in bone tissues. Notably, I emphasize that the diffraction profiles of equatorial and meridional directions of mineralized HAp were in good agreement with those of bone tissues (**Figure 4-15**).

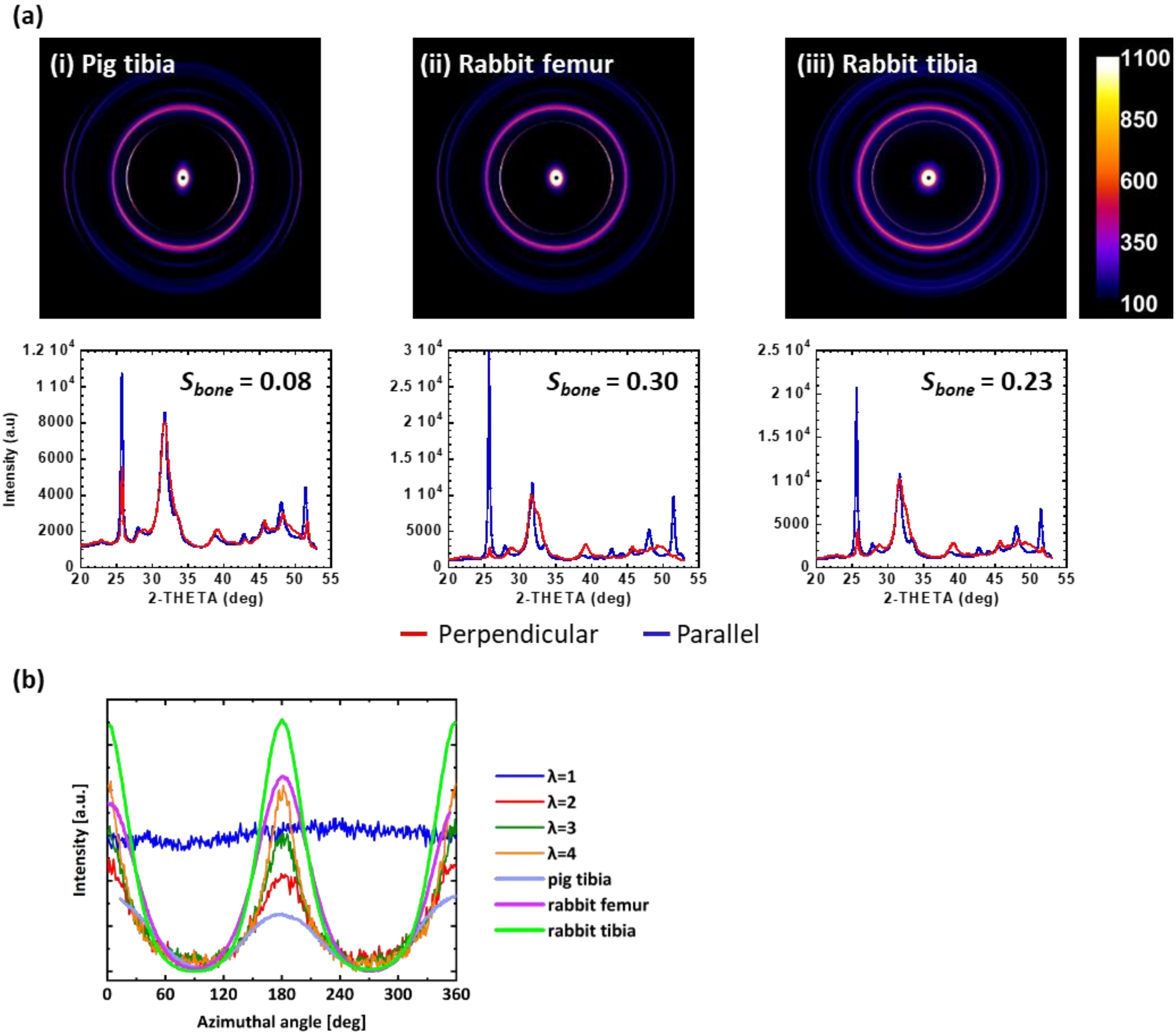

Figure 4-14. (a) 2D diffraction images, and 1D profiles separated in perpendicular (red) and equatorial (blue) directions of cortical regions; (i) pig tibia, (ii) rabbit femur, (iii) rabbit tibia. The orientation degrees *S* of each sample are inserted on the graphs. (b) Azimuthal angle dependences of the WAXD intensity of the HAp (002) plane for HAp/DN gels mineralized at various stretched states and bone tissues. φ = 0 defined by the stretching direction.

Table 4-3. Full width at half maximum (FWHM) from azimuthal angle plot of (002) plane of HAp.

Sample	$\lambda = 1$	$\lambda = 2$	$\lambda = 3$	$\lambda = 4$	Pig tibia	Rabbit femur	Rabbit tibia
FWHM (deg)	-	63.8	46.2	37.1	114.4	69.1	54.8

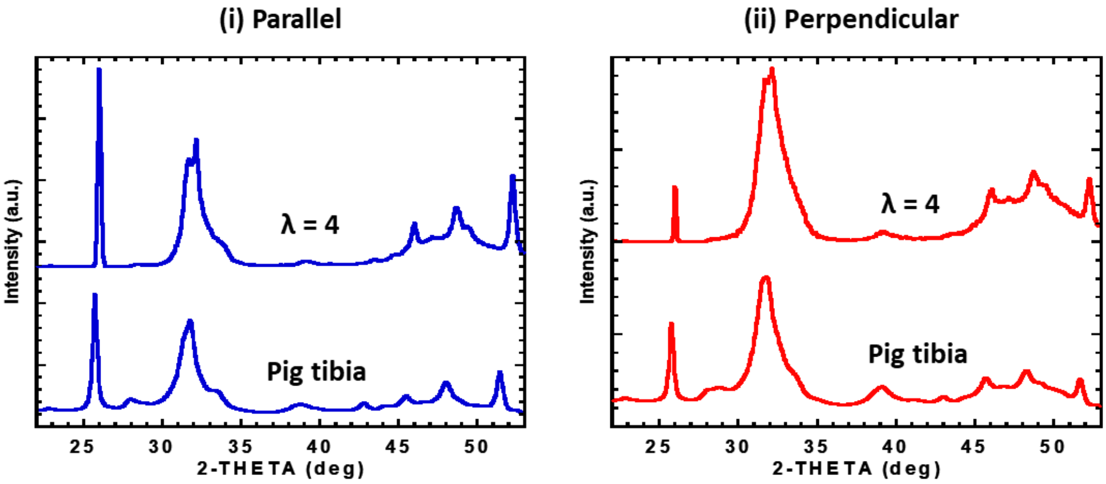

Figure 4-15. Comparison of WAXD 1D profiles between HAp/DN gel mineralized at stretching state (λ= 4) and cortical region of pig tibia for (i) parallel and (ii) perpendicular directions, respectively.

4.3.5 Anisotropic tensile behavior of the stretched HAp/DN gel

Finally, I performed uniaxial tensile test of anisotropic HAp mineralized DN gels in the different directions. The anisotropic HAp mineralized DN gel (λ = 4) was relaxed and cut into dumbbell shapes whose long axe were parallel and perpendicular to the stretching direction of the DN gel matrix. **Figure 4-16(a)** showed stress-strain (S-S) curves of λ = 4 samples parallel and perpendicular to the stretching direction, and λ = 1 sample for HAp/DN gel. The uniaxial tensile results of pristine DN gels pre-stretched at λ = 1, 4 are shown in **Figure 4-16(b)**. Although the pre-stretched pure DN gel (λ = 4) exhibited anisotropy in initial strain region because the first network strands paralleled to stretching direction were fractured more than the perpendicular chains, both S-S curves of λ = 4 parallel and perpendicular samples agreed with that of λ = 1 profile at large strain region. On the other hand, for the HAp/DN samples of λ = 4, both the yield stress and fracture stress of parallel and perpendicular samples showed ascent and descent, respectively, compared with those of λ = 1 sample (**Figure 4-16(a)**). Especially, the fracture stress of λ = 4 parallel was more than double of that of λ = 4 perpendicular. The result indicates that HAp mineralization enhances macroscopic mechanical anisotropy.

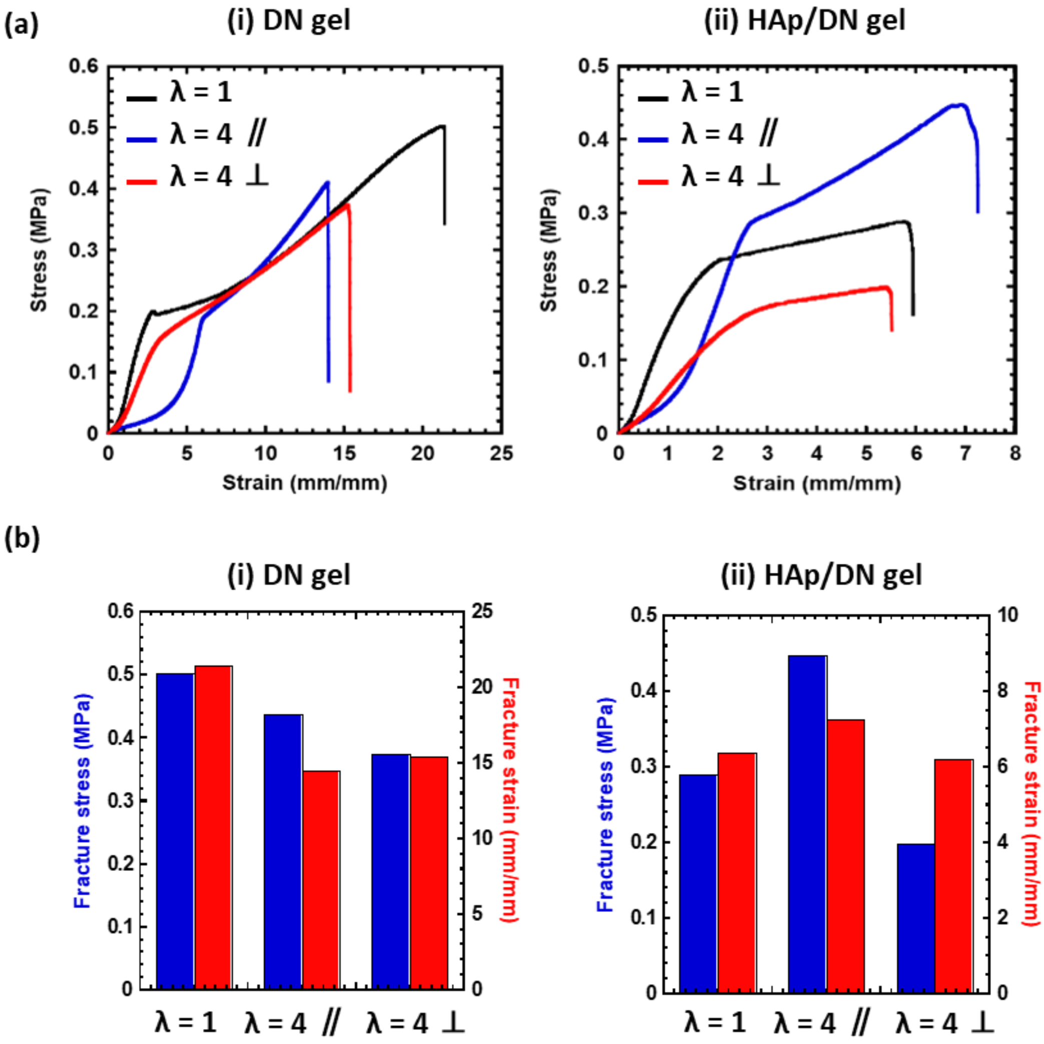

Figure 4-16. (a) Stress-strain curves of (i) HAp/DN gels mineralized at non-stretched state (λ =1) and at stretched state (λ = 4), and (ii) DN gel (λ = 1) and pre-stretched DN gel (λ = 4). (b) Fracture stress and fracture strain of (i) HAp/DN gels mineralized at non-stretched state (λ =1) and at stretched state (λ = 4), and (ii) DN gel (λ = 1) and pre-stretched DN gel (λ = 4).

4.4 Conclusions

I succeeded in developing anisotropic HAp/DN gel with *c*-axis of the crystals preferentially parallel to the stretching direction, by performing the mineralization in stretched DN gels. This method can quantitatively control the orientation of mineralized HAp in DN gel by changing stretch ratio λ. I clarified that the anisotropic crystal growth was regulated not by the molecular level polymer strand orientation but probably by the anisotropic distribution of PAMPS polymer networks in the DN gel. This proposed mechanism gives a strategy to develop anisotropic soft ceramics. Even though the HAp/DN gels do not possess hierarchal structure like bones, the average degree of crystal orientation of the HAp/DN gels in micro-scale achieved to that of bones. Moreover, the mechanical anisotropy was enhanced in the anisotropic HAp/DN gels in comparison to the neat pre-stretched DN gels. This result gives us useful information on develop mechanically anisotropic soft ceramics for various applications, such as bone replacement.

4.5 References

(1) Fukao, K.; Nonoyama, T.; Kiyama, R.; Furusawa, K.; Kurokawa, T.; Nakajima, T.; Gong, J. P. Anisotropic Growth of Hydroxyapatite in Stretched Double Network Hydrogel. ACS Nano 2017, 11 (12), 12103–12110.

(2) Rho, J. Y.; Kuhn-Spearing, L.; Zioupos, P. Mechanical Properties and the Hierarchical Structure of Bone. Medical Engineering and Physics 1998, 20 (2), 92–102.

(3) Mann, S. Biomineralization:Principles and Concepts in Bioinorganic Materials Chemistry; Oxford University Press, 2002.

(4) Gómez-Morales, J.; Iafisco, M.; Delgado-López, J. M.; Sarda, S.; Drouet, C. Progress on the Preparation of Nanocrystalline Apatites and Surface Characterization: Overview of Fundamental and Applied Aspects. Progress in Crystal Growth and Characterization of Materials 2013, 59 (1), 1–46.

(5) Granke, M.; Does, M. D.; Nyman, J. S. The Role of Water Compartments in the Material Properties of Cortical Bone. Calcified Tissue International. 2015, pp 292–307.

(6) Wang, Y.; Azaïs, T.; Robin, M.; Vallée, A.; Catania, C.; Legriel, P.; Pehau-Arnaudet, G.; Babonneau, F.; Giraud-Guille, M. M.; Nassif, N. The Predominant Role of Collagen in the Nucleation, Growth, Structure and Orientation of Bone Apatite. Nature Materials 2012, 11 (8), 724–733.

(7) Nudelman, F.; Pieterse, K.; George, A.; Bomans, P. H. H.; Friedrich, H.; Brylka, L. J.; Hilbers, P. A. J.; De With, G.; Sommerdijk, N. A. J. M. The Role of Collagen in Bone Apatite Formation in the Presence of Hydroxyapatite Nucleation Inhibitors. Nature Materials 2010, 9 (12), 1004–1009.

(8) Roveri, N.; Iafisco, M. Evolving Application of Biomimetic Nanostructured Hydroxyapatite. Nanotechnology, Science and Applications 2010, 3 (1), 107–125.

(9) Fratzl, P.; Weinkamer, R. Nature’s Hierarchical Materials. Progress in Materials Science 2007, 52 (8), 1263–1334.

(10) Weiner, S.; Traub, W. Organization of Hydroxyapatite Crystals within Collagen Fibrils. FEBS Letters 1986, 206 (2), 262–266.

(11) He, G.; Dahl, T.; Veis, A.; George, A. Nucleation of Apatite Crystals in Vitro by Self-Assembled Dentin Matrix Protein 1. Nature Materials 2003, 2 (8), 552–558.

(12) Chen, X.; Wang, W.; Cheng, S.; Dong, B.; Li, C. Y. Mimicking Bone Nanostructure by Combining Block Copolymer Self-Assembly and 1D Crystal Nucleation. ACS Nano 2013, 7 (9), 8251–8257.

(13) Yasuda, K.; Gong, J. P.; Katsuyama, Y.; Nakayama, A.; Tanabe, Y.; Kondo, E.; Ueno, M.; Osada, Y. Biomechanical Properties of High-Toughness Double Network Hydrogels. Biomaterials 2005, 26 (21), 4468–4475.

(14) Yasuda, K.; Kitamura, N.; Gong, J. P.; Arakaki, K.; Kwon, H. J.; Onodera, S.; Chen, Y. M.; Kurokawa, T.; Kanaya, F.; Ohmiya, Y.; et al. A Novel Double-Network Hydrogel Induces Spontaneous Articular Cartilage Regeneration in Vivo in a Large Osteochondral Defect. Macromolecular Bioscience 2009, 9 (4), 307–316.

(15) Nonoyama, T.; Wada, S.; Kiyama, R.; Kitamura, N.; Mredha, M. T. I.; Zhang, X.; Kurokawa, T.; Nakajima, T.; Takagi, Y.; Yasuda, K.; et al. Double-Network Hydrogels Strongly Bondable to Bones by Spontaneous Osteogenesis Penetration. Advanced materials (Deerfield Beach, Fla) 2016, 28 (31), 6740–6745.

(16) Wada, S.; Kitamura, N.; Nonoyama, T.; Kiyama, R.; Kurokawa, T.; Gong, J. P.; Yasuda, K. Hydroxyapatite-Coated Double Network Hydrogel Directly Bondable to the Bone: Biological and Biomechanical Evaluations of the Bonding Property in an Osteochondral Defect. Acta Biomaterialia 2016, 44, 125–134.

(17) Kawai, T.; Ohtsuki, C.; Kamitakahara, M.; Miyazaki, T.; Tanihara, M.; Sakaguchi, Y.; Konagaya, S. Coating of an Apatite Layer on Polyamide Films Containing Sulfonic Groups by a Biomimetic Process. Biomaterials 2004, 25 (19), 4529–4534.

(18) Li, H.; Huang, W.; Zhang, Y.; Zhong, M. Biomimetic Synthesis of Enamel-like

Hydroxyapatite on Self-Assembled Monolayers. Materials Science and Engineering C 2007, 27 (4), 756–761.

(19) Gong, J. P.; Katsuyama, Y.; Kurokawa, T.; Osada, Y. Double-Network Hydrogels with Extremely High Mechanical Strength. Advanced Materials 2003, 15 (14), 1155–1158.

(20) Gong, J. P. Why Are Double Network Hydrogels so Tough? Soft Matter 2010, 6 (12), 2583–2590.

(21) Nakajima, T.; Kurokawa, T.; Ahmed, S.; Wu, W. L.; Gong, J. P. Characterization of Internal Fracture Process of Double Network Hydrogels under Uniaxial Elongation. Soft Matter 2013, 9 (6), 1955–1966.

(22) Na, Y. H.; Kurokawa, T.; Katsuyama, Y.; Tsukeshiba, H.; Gong, J. P.; Osada, Y.; Okabe, S.; Karino, T.; Shibayama, M. Structural Characteristics of Double Network Gels with Extremely High Mechanical Strength. Macromolecules 2004, 37 (14), 5370–5374.

(23) Kikuchi, M.; Ikoma, T.; Itoh, S.; Matsumoto, H. N.; Koyama, Y.; Takakuda, K.; Shinomiya, K.; Tanaka, J. Biomimetic Synthesis of Bone-like Nanocomposites Using the Self-Organization Mechanism of Hydroxyapatite and Collagen. Composites Science and Technology 2004, 64 (6), 819–825.

(24) Alqahtani, H.; Lewis, J. C.; Shirokoff, J. Modeling X-Ray Line Shapes from Asphaltenes. Journal of Physics: Conference Series 2017, 810.

(25) Matsuda, T.; Nakajima, T.; Fukuda, Y.; Hong, W.; Sakai, T.; Kurokawa, T.; Chung, U. Il; Gong, J. P. Yielding Criteria of Double Network Hydrogels. Macromolecules 2016, 49 (5), 1865–1872.

(26) Tachaboonyakiat, W.; Serizawa, T.; Akashi, M. Hydroxyapatite Formation on/in Biodegradable Chitosan Hydrogels by an Alternate Soaking Process. Polymer Journal 2001, 33 (2), 177–181.

(27) Góes, J. C.; Figueiró, S. D.; Oliveira, A. M.; Macedo, A. A. M.; Silva, C. C.; Ricardo, N. M. P. S.; Sombra, A. S. B. Apatite Coating on Anionic and Native Collagen Films by an Alternate Soaking Process. Acta Biomaterialia 2007, 3 (5), 773–778.

(28) Liu, J.; Ye, X.; Wang, H.; Zhu, M.; Wang, B.; Yan, H. The Influence of PH and Temperature on the Morphology of Hydroxyapatite Synthesized by Hydrothermal Method. Ceramics International 2003, 29 (6), 629–633.

(29) Fathi, M. H.; Hanifi, A. Evaluation and Characterization of Nanostructure Hydroxyapatite Powder Prepared by Simple Sol-Gel Method. Materials Letters 2007, 61 (18), 3978–3983.

(30) Qiao, J.; Hamaya, T.; Okada, T. Chemically Modified Poly(Vinyl Alcohol)−Poly(2-Acrylamido-2-Methyl-1-Propanesulfonic Acid) as a Novel Proton-Conducting Fuel Cell Membrane. Chemistry of Materials 2005, 17 (9), 2413–2421.

(31) Diao, H.; Yan, F.; Qiu, L.; Lu, J.; Lu, X.; Lin, B.; Li, Q.; Shang, S.; Liu, W.; Liu, J. High Performance Cross-Linked Poly(2-Acrylamido-2-Methylpropanesulfonic Acid)-Based Proton Exchange Membranes for Fuel Cells. Macromolecules 2010, 43 (15), 6398–6405.

(32) Samuels, R. J. Structured Polymer Properties; John Wiley & Sons, Inc., 1974.

(33) Furusawa, K.; Sato, S.; Masumoto, J. I.; Hanazaki, Y.; Maki, Y.; Dobashi, T.; Yamamoto, T.; Fukui, A.; Sasaki, N. Studies on the Formation Mechanism and the

Structure of the Anisotropic Collagen Gel Prepared by Dialysis-Induced Anisotropic Gelation. Biomacromolecules 2012, 13 (1), 29–39.

(34) Tsukeshiba, H.; Huang, M.; Na, Y. H.; Kurokawa, T.; Kuwabara, R.; Tanaka, Y.; Furukawa, H.; Osada, Y.; Gong, J. P. Effect of Polymer Entanglement on the Toughening of Double Network Hydrogels. Journal of Physical Chemistry B 2005, 109 (34), 16304–16309.

CHAPTER 5: Summary of the dissertation

Using scattering technique, especially small angle X-ray scattering, I revealed structural evolutions of DN gels during uniaxial stretching. This dissertation has described that how and where the first network fractures and why the necking behavior of DN gels occurs related to the mechanical balance between brittle first and soft second networks. And I also explained about the hybridization an anisotropic hydroxyapatite with stretched DN hydrogels based on the formation of bone tissues, considering the structural change in DN gels under uniaxial stretching described in chapter 3.

In the previous observation of the polymer network by scattering techniques, it was difficult to obtain the data of change in structure under highly deforming, because hydrogels are dried during measurement due to long irradiation time. In this dissertation, I overcome this big problem by utilizing the high-brightness in-situ SAXS measurement, which can be obtained data with a measurement time of less than 10 s. Two samples from the same brittle first network but from stretchable second network of different concentration were used for SAXS measurement to the internal fracturing process.

From SAXS analysis, we found that (1) the brittle network shows non-affine deformation even far below the yield strain by local fracture; (2) for the sample of low second network concentration, significant strain amplification occurs around the submicron-scale voids (defects) preexisting in the brittle network, which induces the fracture of brittle network from voids to show necking phenomenon; (3) the strain amplification at voids is suppressed in the sample of high second network concentration, and fracture of brittle network occurs dispersedly without showing the necking. These results show that the fracturing process of the brittle network strongly changes with the second network concentration that controls the stress concentration around the defects.

To apply this internal structural change in DN gels to novel material development, I focused on the bone tissue formation mechanism. In this formation process, the spatially regulated organic template induces the anisotropic HAp growth, and bone tissues achieve the excellent mechanical properties owing to the anisotropic organic/inorganic hybrid structure. From chapter 3, I predicted that the first network formed spatial anisotropic structure in stretched DN gels. As results, HAp mineralized in stretched DN gels grew anisotropically so that the c-axis of HAp was aligned with respect to the stretch direction of DN gels. As increasing the stretch ratio, the orientation degree of HAp increased and was comparable to that of natural bone tissues. Furthermore, the orientation of mineralized HAp with small amount at micro-scale also much affected the mechanical properties of HAp/DN gels at macro-scale.

This dissertation proposed the detail fracturing mechanism on the DN materials for help of developing and understanding the tough material. And I also believe that it can contribute to elucidate the formation process of bioceramics in spatial confinement by polymer network.

List of Publications

Original papers related to doctoral dissertation

1. K. Fukao, T. Nonoyama, R. Kiyama, K. Furusawa, T. Kurokawa, T. Nakajima and J. P. Gong, "Anisotropic Growth of Hydroxyapatite in Stretched Double Network Hydrogel." *ACS Nano* **2017**, 11 (12), 12103–12110.

2. K. Fukao, T. Nakajima, T. Nonoyama, T. Kurokawa, T. Kawai and J. P. Gong, "Effect of Relative Strength of Two Networks on Internal Fracture Process of Double Network Hydrogels as Revealed by in situ Small-Angle X-ray Scattering." *Macromolecules*, **2020** (**Accepted on 24 January 2020**).

Presentation in conferences related to doctoral dissertation

1. K. Fukao, T. Nakajima, T. Nonoyama, T. Kawai and J. P. Gong, "X-ray Scattering Study of Double Network Hydrogels" The 16th Pacific Polymer Conference (PPC16), Singapore, December 2019 (Poster)

2. K. Fukao, T. Nonoyama, T. Nakajima, T. Kawai and J. P. Gong, "Small-Angle X-ray Scattering of Double Network Hydrogels under Uniaxial Stretching" 第 29 回日本 MRS 年次大会, Kanagawa (Tokyo), November 2019 (Poster)

3. K. Fukao, T. Nonoyama, R. Kiyama, K. Furusawa, T. Kawai, T. Kurokawa, T. Nakajima, and J. P. Gong, "Mineralization of Anisotropic Hydroxyapatite on Stretched High-Toughness Hydrogel" The 13th Pacific Rim Conference of Ceramic Societies (PACRIM13), Okinawa (Japan), October 2019 (Oral)

4. K. Fukao, T. Nonoyama, T. Nakajima, T. Kawai and J. P. Gong, “In-situ X-ray scattering study of Double Network Gels under Uniaxial Stretching” 第32回日本放射光学会年会・放射光科学合同シンポジウム, Fukuoka (Japan), January 2019 (Poster)

5. K. Fukao, T. Nonoyama, T. Nakajima, T. Kawai and J. P. Gong, “In-situ X-ray scattering study of Double Network Gels under Uniaxial Stretching” 第28回日本MRS年次大会, Fukuoka (Japan), December 2018 (Poster)

6. K. Fukao, T. Nonoyama, T. Nakajima, T. Kurokawa and J. P. Gong, “X線散乱法によるDouble Networkゲルの延伸過程における内部構造の評価” 第27回ポリマー材料フォーラム, Tokyo (Japan), November, 2018 (invited poster)

7. K. Fukao, T. Nonoyama, T. Nakajima, T. Kurokawa, T. Kawai and J. P. Gong, “一軸延伸過程におけるダブルネットワークゲルのin-situ小角X線散乱” 第67回高分子討論会, Hokkaido (Japan), September, 2018 (Poster)

8. K. Fukao, T. Nonoyama, T. Nakajima, T. Kurokawa and J. P. Gong, “X線散乱法によるDouble Networkゲルの延伸過程における内部構造の評価” 第67回高分子学会年次大会, Nagoya (Japan), May, 2018 (Poster)

9. K. Fukao, T. Nonoyama, K. Furusawa, Kurokawa, T. Nakajima, and J. P. Gong, “伸

長下ハイドロゲル内におけるハイドロキシアパタイトの異方的結晶成長”
日本セラミックス協会 2018 年年会, Miyagi (Japan), March 2018 (Poster)

10. K. Fukao, T. Nonoyama, R. Kiyama, K. Furusawa, T. Kurokawa, T. Nakajima, and J. P. Gong, “Anisotropic Crystal Growth of Hydroxyapatite induced by Stretched High-Toughness Hydrogel” 7th Academic Exchange Collaborational Research ETH Zurich-Hokkaido University, Zurich, (Swiss), November 2017 (Oral)

11. K. Fukao, T. Nonoyama, Kurokawa, T. Nakajima, and J. P. Gong, “Anisotropic Growth of Hydroxyapatite in Elongated Double Network Gel” Hokkaido University-ImPACT Joint Symposium on Advanced Soft Matter: From Single Molecule to Tough Polymers, Sapporo (Japan), August 2017 (Poster)

12. K. Fukao, T. Nonoyama, K. Furusawa, T. Kurokawa, T. Nakajima, and J. P. Gong, “異方的高分子網目空間におけるバイオミネラリゼーション” 日本バイオマテリアル学会北海道ブロック第 2 回研究会, Hokkaido (Japan), May 2017 (Poster)

Presentation in conferences (others)

1. <u>K. Fukao</u>, Y. Meier, T. Nakajima, T. Nonoyama, and J. P. Gong, “ダブルネットワークゲルの強靭化に対する網目間相互作用の効果” 第 68 回高分子学会年次大会, Osaka (Japan), May 2019 (Poster)

Acknowledgement

This research on this dissertation has been carried out in the Laboratory of Soft and Wet Matter (LSW), Graduate School of Life Science, Hokkaido University, Japan, supervised by Professor Jian Ping Gong. Associate examiners are Professor Takayuki Kurokawa, Professor Min Yao and Assistant Professor Takayuki Nonoyama.

Firstly, I greatly appreciate all the support and encouragement of my respected supervisor, Professor Jian Ping Gong during my bachelor's, master's and doctoral study in LSW. She gave me not only her tremendous academic support to be an outstanding researcher but also so many wonderful opportunities. I really appreciate that she evaluated my doctoral research, and through a lot of discussions with her, I could acquire a deep understanding of polymer materials and an ability to perform research. I really respect her positive attitude, research understanding and considering.

I would like to many thanks also to Professor Takayuki Kurokawa, Associate Professor Tasuku Nakajima, Assistant Professor Takayuki Nonoyama, Tenure Track Assistant Professor Daniel R. King and Assistant Professor Kunpeng Cui for their helpful scientific comments, fruitful discussions and useful suggestions regarding my research. I am also very grateful to post-doctoral fellows, guest researcher and research assistants in "LSW", especially, Dr. Yoshinori Katsuyama gave me a lot of advices and helps for production of equipment required for conducting my doctoral research. I also would like to thank the staffs in LSW; Ms. Eiko Hasegawa, Ms. Yuki Okubo, Ms Kato and Ms. Iseya for helping me in financial works and lab life of Hokkaido University.

I would like to say a very big thank you to Associate Professor Kazuya Furusawa in Fukui University of Technology and Assistant Professor Takahiko Kawai in Gunma University for the kind support on the detailed analysis of X-ray diffraction and scattering measurement. I also would like to thank the staffs in RIKEN (Dr. Taiki Hoshino, Dr. So Fujinami, and Dr. Tomotaka Nakatani) for their kind assistance with the SAXS measurement at SPring-8.

I want to gratefully acknowledge Hokkaido University's "Ambitious Leader's Program" supported by MEXT, Japan for supporting my research. It was impossible to complete my doctoral research without their financial support and fruitful opportunity. Participating in the Ambitious Leader's Program is a valuable experience to acquire knowledge not only for research but also for an attitude as a member of society.

Finally, special thanks to my family for all the support and encouragement during the life in Hokkaido University. I dedicate this dissertation to them.

Kazuki Fukao
Laboratory of Soft & Wet Matter
Graduate School of Life Science
Hokkaido University
Sapporo Japan

March 2020